# END-TO-END OPTIMIZED IMAGE COMPRESSION

**Johannes Ballé***
Center for Neural Science
New York University
New York, NY 10003, USA
johannes.balle@nyu.edu

**Valero Laparra**
Image Processing Laboratory
Universitat de València
46980 Paterna, Spain
valero.laparra@uv.es

**Eero P. Simoncelli***
Center for Neural Science and Courant Institute of Mathematical Sciences
New York University
New York, NY 10003, USA
eero.simoncelli@nyu.edu

## ABSTRACT

We describe an image compression system, consisting of a nonlinear encoding transformation, a uniform quantizer, and a nonlinear decoding transformation. The transforms are constructed in three successive layers of convolutional linear filters and nonlinear activation functions, but unlike most convolutional neural networks, we use a joint nonlinearity that implements a form of local gain control, inspired by those used to model biological neurons. Using a variant of stochastic gradient descent, we jointly optimize the entire system for rate–distortion performance over a database of training images, introducing a continuous proxy for the discontinuous loss function arising from the quantizer. The relaxed optimization problem resembles that of variational autoencoders, except that it must operate at any point along the rate–distortion curve, whereas the optimization of generative models aims only to minimize entropy of the data under the model. Across an independent set of test images, we find that the optimized coder generally exhibits better rate–distortion performance than the standard JPEG and JPEG 2000 compression systems. More importantly, we observe a dramatic improvement in visual quality for all images at all bit rates.

## 1 INTRODUCTION

Data compression is a fundamental and well-studied problem in engineering, and is commonly formulated with the goal of designing codes for a given discrete data ensemble with minimal entropy (Shannon, 1948). The solution relies heavily on knowledge of the probabilistic structure of the data, and thus the problem is closely related to probabilistic source modeling. However, since all practical codes must have finite entropy, continuous-valued data (such as vectors of image pixel intensities) must be quantized to a finite set of discrete values, which introduces error. In this context, known as the *lossy compression problem*, one must trade off two competing costs: the entropy of the discretized representation (*rate*) and the error arising from the quantization (*distortion*). Different compression applications, such as data storage or transmission over limited-capacity channels, impose different rate–distortion trade-offs.

Joint optimization of rate and distortion is difficult. Without further constraints, the general problem of optimal vector quantization is intractable in high dimensions (Gersho and Gray, 1992). For this reason, most existing image compression systems operate by linearly transforming the data vector into a suitable continuous-valued representation, quantizing its elements independently, and then encoding the resulting discrete representation using a lossless *entropy code* (Wintz, 1972; Netravali and Limb, 1980). For example, JPEG uses a discrete cosine transform on blocks of pixels, and JPEG 2000 uses a multi-scale orthogonal wavelet decomposition. Typically, the three components

*JB and EPS are supported by the Howard Hughes Medical Institute.

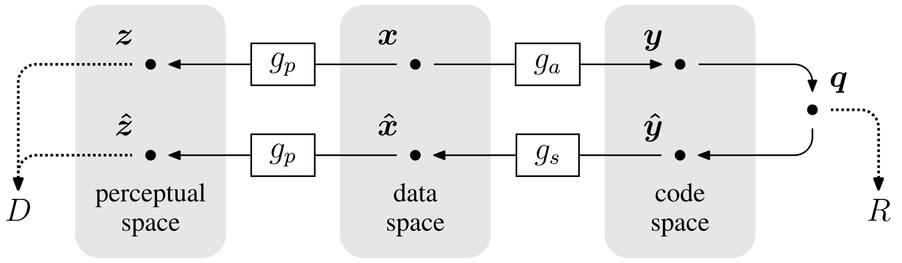

Figure 1: General framework for rate–distortion optimization of nonlinear transform coding (Ballé, Laparra, and Simoncelli, 2016). A vector of image intensities $\boldsymbol{x} \in \mathbb{R}^N$ is mapped to a latent *code space* via a parametric multivariate *analysis* transform, $\boldsymbol{y} = g_a(\boldsymbol{x}; \boldsymbol{\phi})$. This representation is quantized, yielding a discrete-valued vector $\boldsymbol{q} \in \mathbb{Z}^M$ which is then compressed. The *rate* of this discrete code, $R$, is lower bounded by the entropy of the discrete probability distribution of the quantized vector, $H[P_{\boldsymbol{q}}]$. To reconstruct the compressed image, the discrete elements of $\boldsymbol{q}$ are reinterpreted as a continuous-valued vector $\hat{\boldsymbol{y}}$, which is transformed back to the data space using a parametric *synthesis* transform $\hat{\boldsymbol{x}} = g_s(\hat{\boldsymbol{y}}; \boldsymbol{\theta})$. Distortion is assessed by transforming to a *perceptual space* using a (fixed) transform, $\hat{\boldsymbol{z}} = g_p(\hat{\boldsymbol{x}})$, and evaluating a metric $d(\boldsymbol{z}, \hat{\boldsymbol{z}})$. The parameter vectors $\boldsymbol{\phi}$ and $\boldsymbol{\theta}$ are optimized for a weighted sum of the rate and distortion measures over a set of images.

of transform coding systems – the transform, the quantizer, and the entropy coder – are separately optimized (often through manual parameter adjustment).

We have developed a framework for end-to-end optimization of an image compression system based on nonlinear transforms (figure 1). Previously, we demonstrated that a system consisting of linear–nonlinear block transformations, optimized for a measure of perceptual distortion, exhibited visually superior performance compared to a system optimized for mean squared error (MSE) (Ballé, Laparra, and Simoncelli, 2016). Here, we optimize for MSE, and focus on the use of more flexible transforms built from cascades of linear convolutions and nonlinearities. Specifically, we use a generalized divisive normalization (GDN) joint nonlinearity that is inspired by models of neurons in biological visual systems, and has proven effective in Gaussianizing image densities (Ballé, Laparra, and Simoncelli, 2015). This cascaded transformation is followed by uniform scalar quantization (i.e., each element is rounded to the nearest integer), which effectively implements a parametric form of vector quantization on the original image space. The compressed image is reconstructed from these quantized values using an approximate parametric nonlinear inverse transform.

For any desired point along the rate–distortion curve, the parameters of both forward and inverse transforms are jointly optimized using stochastic gradient descent. To achieve this in the presence of quantization (which produces zero gradients almost everywhere), we use a proxy loss function based on a continuous relaxation of the probability model, replacing the quantization step with additive uniform noise. The relaxed rate–distortion optimization problem bears some resemblance to those used to learn generative image models, and in particular variational autoencoders (Kingma and Welling, 2014; Rezende, Mohamed, and Wierstra, 2014), but differs in the constraints we impose to ensure that it approximates the discrete problem all along the rate–distortion curve. Finally, rather than reporting discrete entropy estimates, we implement an entropy coder and report performance values using the actual bit rate, thus demonstrating the feasibility of our solution as a complete lossy compression system.

## 2 Optimization of nonlinear transform coding

Our objective is to minimize a weighted sum of the rate and distortion, $R + \lambda D$, over analysis and synthesis transforms and the entropy code, where parameter $\lambda$ governs the trade-off between the two terms (figure 2, left panel). The actual rates achieved by a properly designed entropy code are only slightly larger than the discrete entropy (Rissanen and Langdon, 1981), and thus we define the objective functional directly in terms of entropy:

$$L[g_a, g_s] = -\,\mathbb{E}\big[\log_2 P_{\boldsymbol{q}}\big] + \lambda\,\mathbb{E}\big[d(\boldsymbol{z}, \hat{\boldsymbol{z}})\big], \tag{1}$$

where both expectations can be approximated by averages over a training set of images. Since optimal quantization is difficult in high dimensional spaces, we instead assume a fixed uniform scalar

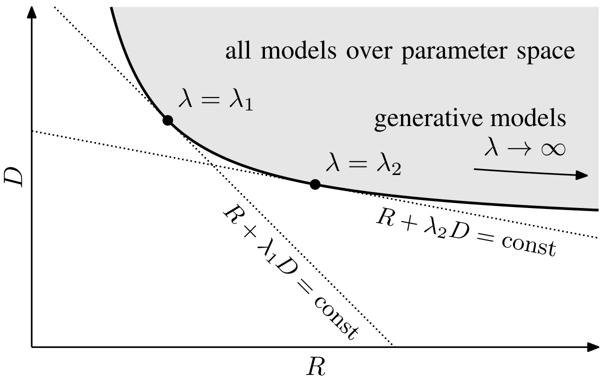
all models over parameter space
$\lambda = \lambda_1$
generative models
$\lambda \to \infty$
$\lambda = \lambda_2$
$R + \lambda_2 D = \text{const}$
$R + \lambda_1 D = \text{const}$
$D$
$R$

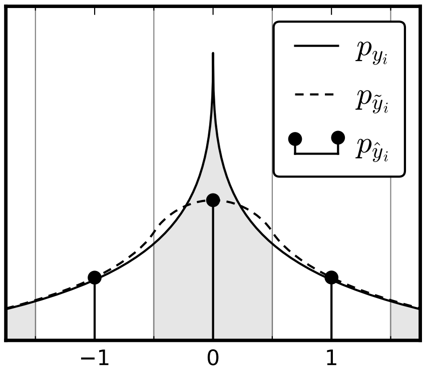

Figure 2: Left: The rate–distortion trade-off. The gray region represents the set of all rate–distortion values that can be achieved with a given model (over all possible parameter settings). Right: One-dimensional illustration of relationship between densities of $y_i$ (elements of latent representation), $\hat{y}_i$ (quantized elements), and $\tilde{y}_i$ (elements perturbed by uniform noise). Each discrete probability value in $p_{\hat{y}_i}$ corresponds to the portion of the density $p_{y_i}$ within the corresponding quantization bin (indicated by shading). Density $p_{\tilde{y}_i}$ provides a continuous interpolated function that is consistent with the discrete probability $p_{\hat{y}_i}$ at integer values.

quantizer, and aim to have the nonlinear transformations warp the code space in an appropriate way, effectively implementing a parametric form of vector quantization. Given a powerful enough set of transformations, we can assume without loss of generality that the quantization bin size is always one and the representing values are at the center of the bins. That is,

$$\hat{y}_i = q_i = \operatorname{round}(y_i). \tag{2}$$

The marginal density of $\hat{y}_i$ is then given by a train of discrete probability masses (Dirac delta functions, figure 2, right panel) with weights equal to the probability mass function of $q_i$:

$$P_{q_i}(n) = \int_{n-\frac{1}{2}}^{n+\frac{1}{2}} p_{y_i}(t)\, \mathrm{d}t, \qquad \text{for all } n \in \mathbb{Z}, \tag{3}$$

Note that both terms in (1) depend on the quantized values, and the derivatives of the quantization function (2) are zero almost everywhere, rendering gradient descent ineffective. To allow optimization via stochastic gradient descent, we replace the quantizer with an additive i.i.d. uniform noise source $\Delta\boldsymbol{y}$, which has the same width as the quantization bins (one). This relaxed formulation has two desirable properties. First, the density function of $\tilde{\boldsymbol{y}} = \boldsymbol{y} + \Delta\boldsymbol{y}$ is a continuous relaxation of the probability mass function of $\boldsymbol{q}$ (figure 2, right panel):

$$p_{\tilde{\boldsymbol{y}}}(\boldsymbol{n}) = P_{\boldsymbol{q}}(\boldsymbol{n}), \qquad \text{for all } \boldsymbol{n} \in \mathbb{Z}^M, \tag{4}$$

which implies that the differential entropy of $\tilde{\boldsymbol{y}}$ can be used as an approximation of the discrete entropy of $\boldsymbol{q}$. Second, independent uniform noise approximates quantization error in terms of its marginal moments, and is frequently used as a model of quantization error (Gray and Neuhoff, 1998). We can thus use the same approximation for our measure of distortion. We examine the empirical quality of these rate and distortion approximations in section 4.

Because model error can have an effect on the approximation, we use unbiased, frequentist model estimates of $p_{\tilde{\boldsymbol{y}}}$ rather than Bayesian estimates (details in the appendix). Further, we assume independent marginals in the code space for both the relaxed probability model and the entropy code, and model the marginals $p_{\tilde{y}_i}$ non-parametrically. Specifically, we use finely sampled piecewise linear functions (see appendix). Since $p_{\tilde{y}_i} = p_{y_i} * \mathcal{U}(0,1)$ is effectively smoothed by a box-car filter – the uniform density on the unit interval, $\mathcal{U}(0,1)$ – the model error can be made arbitrarily small by decreasing the sampling interval.

Given this continuous approximation of the quantized coefficient distribution, the loss function for parameters $\boldsymbol{\theta}$ and $\boldsymbol{\phi}$ can be written as:

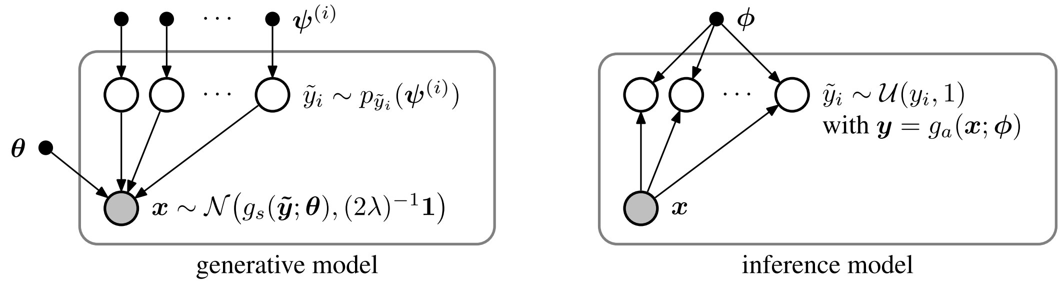

$\boldsymbol{\psi}^{(i)}$
$\tilde{y}_i \sim p_{\tilde{y}_i}(\boldsymbol{\psi}^{(i)})$
$\boldsymbol{\theta}$
$\boldsymbol{x} \sim \mathcal{N}\big(g_s(\tilde{\boldsymbol{y}}; \boldsymbol{\theta}), (2\lambda)^{-1}\mathbf{1}\big)$
generative model
$\boldsymbol{\phi}$
$\tilde{y}_i \sim \mathcal{U}(y_i, 1)$
with $\boldsymbol{y} = g_a(\boldsymbol{x}; \boldsymbol{\phi})$
$\boldsymbol{x}$
inference model

Figure 3: Probabilistic graphical model representation of the relaxed rate–distortion optimization problem, which is analogous to that used for variational autoencoders.

$$L(\boldsymbol{\theta}, \boldsymbol{\phi}) = \mathbb{E}_{\boldsymbol{x},\Delta\boldsymbol{y}}\Bigg[-\sum_i \log_2 p_{\tilde{y}_i}(g_a(\boldsymbol{x}; \boldsymbol{\phi}) + \Delta\boldsymbol{y}; \boldsymbol{\psi}^{(i)}) + \lambda\, d\Big(g_p\big(g_s(g_a(\boldsymbol{x}; \boldsymbol{\phi}) + \Delta\boldsymbol{y}; \boldsymbol{\theta})\big), g_p(\boldsymbol{x})\Big)\Bigg]. \tag{5}$$

where vector $\boldsymbol{\psi}^{(i)}$ parameterizes the piecewise linear approximation of $p_{\tilde{y}_i}$. This is continuous and differentiable with respect to the parameters, and thus well-suited for stochastic optimization.

## 2.1 Relationship to generative image models

We derived our formulation directly from the classical rate–distortion optimization problem. However, once the transition to a continuous loss function is made, the optimization problem resembles those encountered in fitting generative models of images, and can more specifically be cast in the context of variational autoencoders (Kingma and Welling, 2014; Rezende, Mohamed, and Wierstra, 2014). In Bayesian variational inference, we are given an ensemble of observations of a random variable $x$ along with a generative model $p_{x|y}(x|y)$. We seek to find a posterior $p_{y|x}(y|x)$, which generally cannot be expressed in closed form. The approach followed by Kingma and Welling (2014) consists of approximating this posterior with a density $q(y|x)$, by minimizing the Kullback–Leibler divergence between the two:

$$\begin{aligned} D_{\mathrm{KL}}\big[q \| p_{y|x}\big] &= \mathbb{E}_{y\sim q} \log q(y|x) - \mathbb{E}_{y\sim q} \log p_{y|x}(y|x) \\ &= \mathbb{E}_{y\sim q} \log q(y|x) - \mathbb{E}_{y\sim q} \log p_{x|y}(x|y) - \mathbb{E}_{y\sim q} \log p_y(y) + \text{const.} \end{aligned} \tag{6}$$

This objective function is equivalent to our relaxed rate–distortion optimization problem, with distortion measured as MSE, if we define the generative model as follows (figure 3):

$$p_{\boldsymbol{x}|\tilde{\boldsymbol{y}}}(\boldsymbol{x}|\tilde{\boldsymbol{y}}; \lambda, \boldsymbol{\theta}) = \mathcal{N}\big(\boldsymbol{x}; g_s(\tilde{\boldsymbol{y}}; \boldsymbol{\theta}), (2\lambda)^{-1}\mathbf{1}\big), \tag{7}$$

$$p_{\tilde{\boldsymbol{y}}}(\tilde{\boldsymbol{y}}; \boldsymbol{\psi}^{(0)}, \boldsymbol{\psi}^{(1)}, \dots) = \prod_i p_{\tilde{y}_i}(\tilde{y}_i; \boldsymbol{\psi}^{(i)}), \tag{8}$$

and the approximate posterior as follows:

$$q(\tilde{\boldsymbol{y}}|\boldsymbol{x}; \boldsymbol{\phi}) = \prod_i \mathcal{U}(\tilde{y}_i; y_i, 1) \quad \text{with } \boldsymbol{y} = g_a(\boldsymbol{x}; \boldsymbol{\phi}), \tag{9}$$

where $\mathcal{U}(\tilde{y}_i; y_i, 1)$ is the uniform density on the unit interval centered on $y_i$. With this, the first term in the Kullback–Leibler divergence is constant; the second term corresponds to the distortion, and the third term corresponds to the rate (both up to additive constants). Note that if a perceptual transform $g_p$ is used, or the metric $d$ is not Euclidean, $p_{\boldsymbol{x}|\tilde{\boldsymbol{y}}}$ is no longer Gaussian. The equivalence to variational autoencoders cannot be guaranteed in general, as the distortion term may not correspond to a normalizable density. At least for any affine and invertible perceptual transform and any translation-invariant metric, it can be shown to correspond to the density

$$p_{\boldsymbol{x}|\tilde{\boldsymbol{y}}}(\boldsymbol{x}|\tilde{\boldsymbol{y}}; \lambda, \boldsymbol{\theta}) = \frac{1}{Z(\lambda)} \exp\Bigg(-\lambda\, d\Big(g_p\big(g_s(\tilde{\boldsymbol{y}}; \boldsymbol{\theta})\big), g_p(\boldsymbol{x})\Big)\Bigg), \tag{10}$$

where $Z(\lambda)$ normalizes the density (but need not be computed to fit the model).

Despite these similarities between our compression framework and that of variational autoencoders, it is worth noting that the role of discretization in lossy compression systems leads to fundamental differences. First, naively discretizing a continuous representation may severely compromise its effectiveness for compression, however well it may perform as a generative model. For example, performing scalar quantization on multivariate data is not even guaranteed to be optimal if the data is marginally independent and the error metric is separable (Gersho and Gray, 1992). For the purpose of evaluation, certain precautions must be taken to be able to compare differential entropy with (discrete) entropy, and discrete entropy can only be reasonably equated to the actual rate of a discrete code if an accurate discrete probability model is available to design the code.

Second, generative models aim to minimize differential entropy of the data ensemble under the model, i.e., explaining fluctuations in the data. This often means minimizing the variance of a "slack" term like (7), which in turn *maximizes* $\lambda$. Lossy compression methods, on the other hand, are optimized to achieve the best trade-off between having the model explain the data (which increases rate and decreases distortion), and having the slack term explain the data (which decreases rate and increases distortion). The overall performance of a compression model is determined by the shape of the convex hull of attainable model distortions and rates, over all possible values of the model parameters. Finding this convex hull is equivalent to optimizing the model for *particular* values of $\lambda$ (see figure 2). In contrast, generative models operate in a regime where $\lambda$ is inferred and ideally approaches infinity for noiseless data. This is the regime of lossless compression. Even so, lossless compression methods still need to operate in a discretized space, typically directly on quantized luminance values. For generative models, the discretization of luminance values is usually considered a nuisance (Theis, van den Oord, and Bethge, 2015), although there are examples of generative models that operate on quantized pixel values (van den Oord, Kalchbrenner, and Kavukcuoglu, 2016).

Finally, correspondence between the typical slack term (7) of a generative model (figure 3, left panel) and the distortion metric in rate–distortion optimization holds for simple metrics, such as the Euclidean distance. A more general perceptual measure would be considered a peculiar choice from a generative modeling perspective, if it corresponds to a density at all.

## 3 Choice of forward, inverse, and perceptual transforms

We applied our optimization framework to analysis/synthesis transforms constructed from linear–nonlinear cascades. Most compression systems are based on orthogonal linear transforms, chosen to reduce correlations in the data, which substantially simplifies entropy coding. But the joint statistics of linear filter responses exhibit strong higher-order dependencies. These may be significantly reduced through the use of a joint nonlinear gain control operations (Schwartz and Simoncelli, 2001; Lyu, 2010; Sinz and Bethge, 2013), inspired by models of visual neurons (Heeger, 1992; Carandini and Heeger, 2012). Earlier results suggested that incorporating local normalization in cascaded convolutional neural networks can improve performance in object recognition (Jarrett et al., 2009), although the normalization parameters in this case were not optimized. Here, we make use of a generalized divisive normalization (GDN) transform that we have previously shown to be highly efficient in Gaussianizing the local joint statistics of natural images, much more so than cascades of linear transforms followed by marginal nonlinearities (Ballé, Laparra, and Simoncelli, 2015). Specifically, our analysis transform $g_a$, consists of three stages of convolution, subsampling, and GDN, with the latter defined as:

$$v_i = \frac{u_i}{\left(\beta_i + \sum_j \gamma_{ij} u_j^2\right)^{\frac{1}{2}}}, \tag{11}$$

where the vectors $\boldsymbol{u}$ and $\boldsymbol{v}$ hold the linear and normalized activations at one spatial location across feature maps, respectively, and the vector $\boldsymbol{\beta}$ and the symmetric matrix $\boldsymbol{\gamma}$ are parameters to be optimized. The synthesis transform $g_s$ is formed as an approximate inverse (specifically, it uses one step of the fixed point iteration that can be used to invert the GDN transform):

$$v_i = u_i \cdot \left(\beta_i + \sum_j \gamma_{ij} u_j^2\right)^{\frac{1}{2}}, \tag{12}$$

with all parameters defined in the same way as the GDN parameters, but separately optimized.

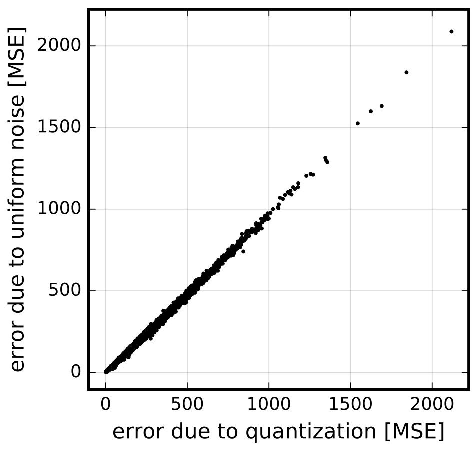

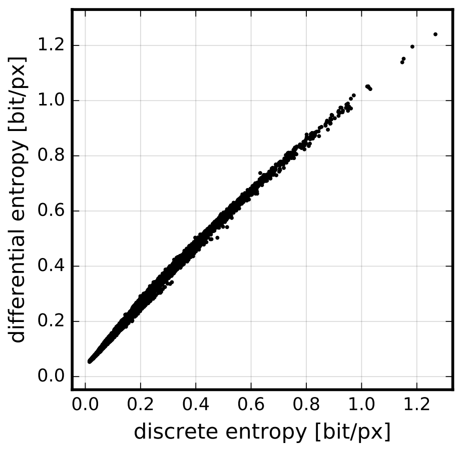

Figure 4: Scatter plots comparing discrete vs. continuously-relaxed values of the two terms of the objective function, evaluated for the optimized GDN model. Points correspond to different values of $\lambda$ between 32 and 2048 (inclusive), for images drawn from a random subset of 2169 images (one third) from the training set. Left: distortion term, evaluated for $g_s(\hat{\boldsymbol{y}})$ vs. $g_s(\tilde{\boldsymbol{y}})$. Right: rate term, $H[P_{q_i}]$ vs. $h[p_{\tilde{y}_i}]$ (summed over $i$).

For the convolutional structure of our grayscale analysis transform, we use 128 filters in the first stage, each sampled by a factor of 4 vertically and horizontally, with the remaining two stages using 128 filters operating over the input features from previous stages, and subsampled by factors of 2 in each direction. The net output thus has half the dimensionality of the input. The synthesis transform is structured analogously. For the two highest values of $\lambda$, and for RGB models, we increased the network capacity by increasing the number of filters in each stage to 256 and 192, respectively.

In previous work, we used a perceptual transform $g_p$ separately optimized to mimic human judgements of grayscale image distortions (Laparra et al., 2016), and showed that a set of one-stage transforms optimized for this distortion measure led to visually improved results (Ballé, Laparra, and Simoncelli, 2016). Here, we set the perceptual transform $g_p$ to the identity, and use mean squared error (MSE) as the metric (i.e., $d(\boldsymbol{z}, \tilde{\boldsymbol{z}}) = \|\boldsymbol{z} - \tilde{\boldsymbol{z}}\|_2^2$). This allows a more interpretable comparison to existing coders (which are generally optimized for MSE), and also allows optimization for color images, for which we do not currently have a reliable perceptual metric.

## 4 Experimental results

For training, we used Adam (Kingma and Ba, 2014), a variant of stochastic gradient descent, to jointly optimize the full set of parameters (all linear filters, and normalization parameters of the nonlinearities used in the analysis and synthesis transforms, as well as parameters of the entropy model) over a subset of the ImageNet database (Deng et al., 2009) consisting of 6507 images (see appendix for details).

We first verified that the continuously-relaxed loss function given in section 2 provides a good approximation to the actual rate–distortion values obtained with quantization (figure 4). The relaxed distortion term appears to be mostly unbiased, and exhibits a relatively small variance. The relaxed (differential) entropy provides a somewhat positively biased estimate of the discrete entropy for the coarser quantization regime, but the bias disappears for finer quantization, as expected. Note that since the values of $\lambda$ do not have any intrinsic meaning, but serve only to map out the convex hull of optimal points in the rate–distortion plane (figure 2, left panel), a constant bias in either of the terms would simply alter the effective value of $\lambda$, with no effect on the compression performance.

We compare the rate–distortion performance of our system to two standard coders: JPEG and JPEG 2000. For our system, all images were compressed using uniform quantization (the continuous relaxation using additive noise was used only for training purposes). To make the comparisons more fair, we implemented a simple entropy code based on the context-based adaptive binary arithmetic coding framework (CABAC; Marpe, Schwarz, and Wiegand, 2003). All sideband information needed by the decoder (size of images, value of $\lambda$, etc.) was included in the bit stream (see ap-

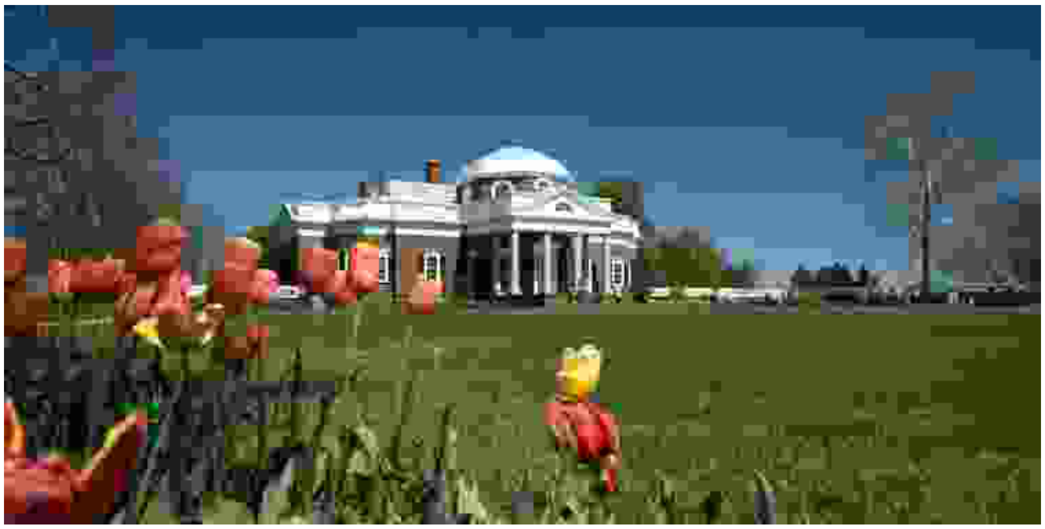
**JPEG**, 4283 bytes (0.121 bit/px), PSNR: 24.85 dB/29.23 dB, MS-SSIM: 0.8079

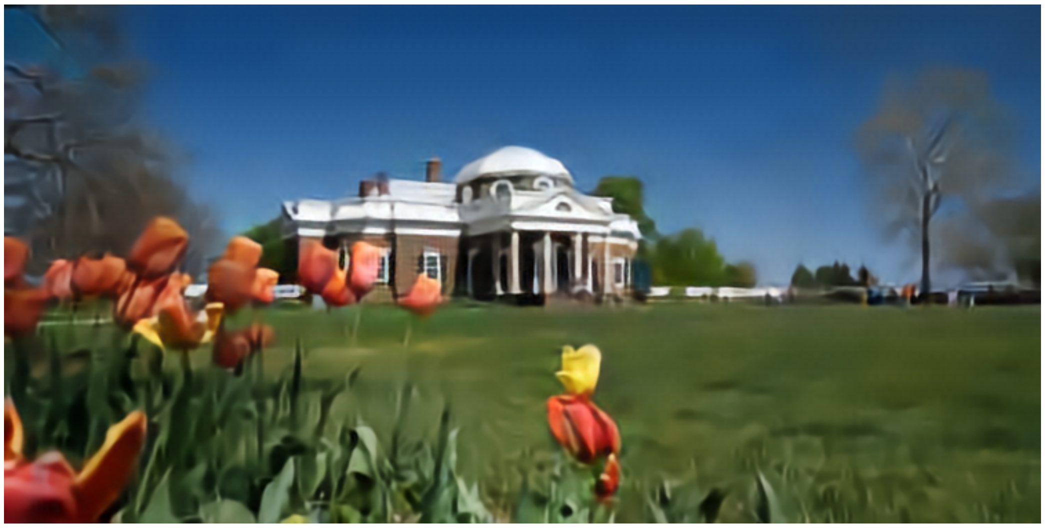
**Proposed method**, 3986 bytes (0.113 bit/px), PSNR: 27.01 dB/34.16 dB, MS-SSIM: 0.9039

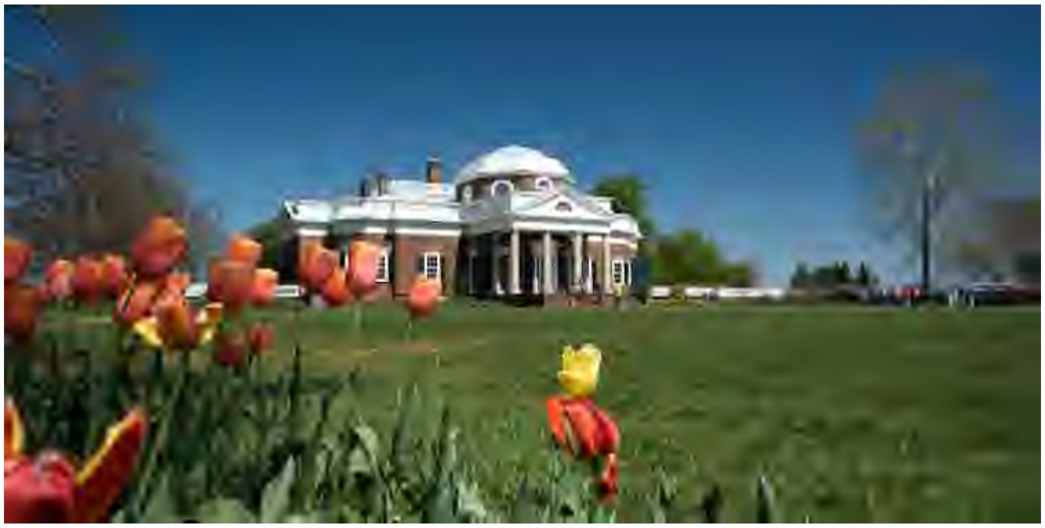
**JPEG 2000**, 4004 bytes (0.113 bit/px), PSNR: 26.61 dB/33.88 dB, MS-SSIM: 0.8860

Figure 5: Heavily compressed example image, 752 $\times$ 376 pixels. Note the appearance of artifacts, especially near edges.

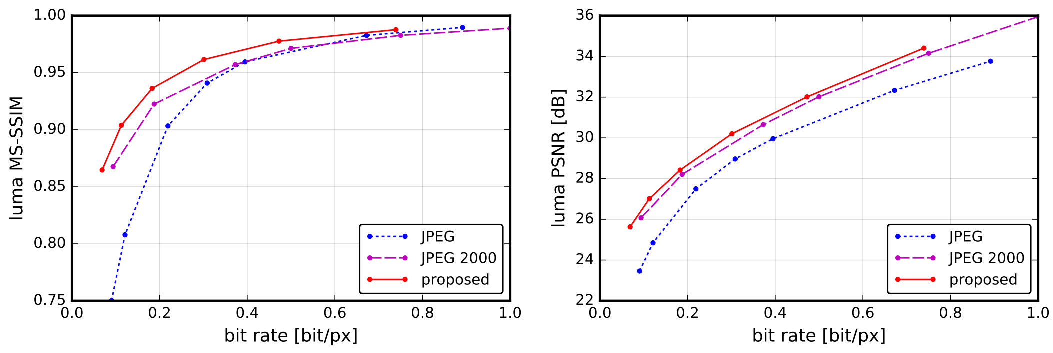

Figure 6: Rate–distortion curves for the luma component of image shown in figure 5. Left: multi-scale structural similarity (MS-SSIM; Wang, Simoncelli, and Bovik (2003)). Right: peak signal-to-noise ratio ($10 \log_{10}(255^2/\text{MSE})$).

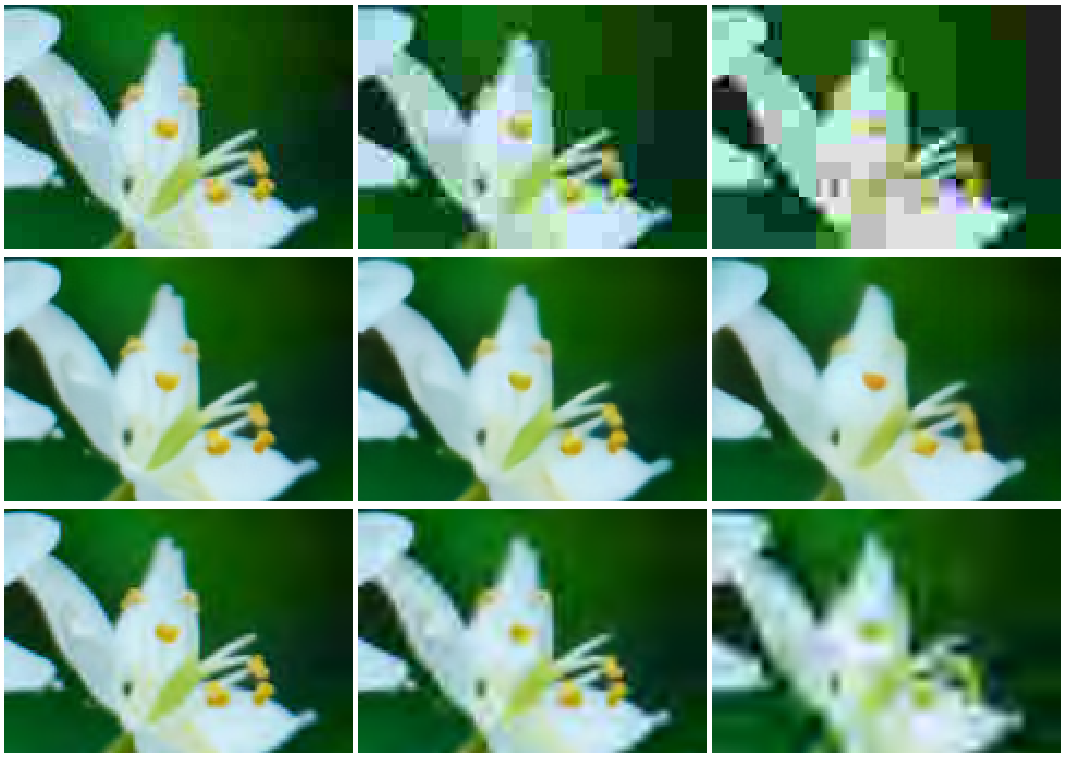

Figure 7: Cropped portion of an image compressed at three different bit rates. Middle row: the proposed method, at three different settings of $\lambda$. Top row: JPEG, with three different quality settings. Bottom row: JPEG 2000, with three different rate settings. Bit rates within each column are matched.

pendix). Note that although the computational costs for training our system are quite high, encoding or decoding an image with the trained system is efficient, requiring only execution of the optimized analysis transformation and quantizer, or the synthesis transformation, respectively. Evaluations were performed on the Kodak image dataset[1], an uncompressed set of images commonly used to evaluate image compression systems. We also examined a set of relatively standard (if outdated) images used by the compression community (known by the names "Lena", "Barbara", "Peppers", and "Mandrill") as well as a set of our own digital photographs. All images, compressed at a variety of bitrates using all three coders, along with their associated rate–distortion curves, are available online at `http://www.cns.nyu.edu/~lcv/iclr2017`.

[1]Downloaded from `http://www.cipr.rpi.edu/resource/stills/kodak.html`

We find that our system, when tested on photographic images not used in training, exhibits better rate–distortion performance than both JPEG and JPEG 2000 for most images, especially at the lower bit rates (although note that results do vary significantly for different images). More importantly, although we use MSE as a distortion metric for training, the appearance of the decoded images is both qualitatively different and substantially improved, exhibiting almost none of the visually disturbing blocking, aliasing, or ringing artifacts commonly seen in images compressed with JPEG, JPEG 2000 and essentially all other compression systems. We find that this visual improvement holds for all images tested, and at all bit rates. Consistent with this, distortion measured with a perceptual metric (MS-SSIM; Wang, Simoncelli, and Bovik, 2003), indicates improvements across all tested images and bit rates (see appendix and online examples).

To demonstrate the qualitative nature of compression artifacts, we show a representative example of a heavily compressed image in figure 5. We show an image compressed using our system for one selected $\lambda$ value, and compare to JPEG/JPEG 2000 images compressed at equal or greater bit rates. The JPEG and JPEG 2000 images exhibit artifacts that are common to all linear transform coders: since local features (edges, contours, texture elements, etc.) are represented using particular combinations of localized linear basis functions, independent scalar quantization of the transform coefficients causes imbalances in these combinations, and leads to visually disturbing blocking, aliasing, and ringing artifacts that reflect the underlying basis. For the proposed system, we see that compressed images are less detailed than the original, with fine texture and other patterns often eliminated altogether, but this is accomplished in a way that preserves the smoothness and sharpness of many contours and edges, giving them a more natural appearance.

The progression from high to low bit rates is visualized in figure 7. The linear coders degrade their approximation of the original image by coarsening the precision of the coefficients of linear basis functions, thus exposing the visual appearance of those basis functions at low bit rates. On the other hand, our method appears to progressively simplify contours and other image features, effectively concealing the quantized nature of the representation.

## 5 Discussion

We have presented a complete image compression system based on nonlinear transform coding, and a methodology to optimize it end-to-end for rate–distortion performance. The system offers significant improvements in rate–distortion performance over JPEG and JPEG 2000 for most images and bitrates. More remarkably, although the system was optimized using mean squared error as a distortion metric, the compressed images are much more natural in appearance than those compressed with JPEG or JPEG 2000, both of which suffer from the severe artifacts commonly seen in linear transform coding methods. Consistent with this, MS-SSIM values show substantial improvement across all images and bitrates that we have examined. We think this is because these cascaded nonlinear transformations have been optimized to capture the features and attributes of images that are represented in the statistics of the data, parallel to the processes of evolution and development that are believed to have shaped visual representations within the human brain (Simoncelli and B. Olshausen, 2001). Nevertheless, additional visual improvements might be possible if the system were trained using a perceptual metric in place of MSE (Ballé, Laparra, and Simoncelli, 2016).

For comparison to standard linear transform coders, we can interpret our analysis transform as a single-stage linear transform followed by a complex vector quantizer. As in many other learned representations (e.g., sparse coding; Lewicki and B. A. Olshausen, 1998), as well as many engineered representations (e.g., the steerable pyramid, Simoncelli, Freeman, et al., 1992; curvelets, Candès and Donoho, 2002; and dual-tree complex wavelets, Selesnick, Baraniuk, and Kingsbury, 2005), the filters in this first stage are localized and oriented and the representation is *overcomplete* (128 filters, each subsampled by a factor of 16). Whereas most transform coders use complete (often orthogonal) linear transforms with spatially separable filters, the overcompleteness and orientation tuning of our initial transform may explain the ability of the system to better represent features and contours with continuously varying orientation, position and scale (Simoncelli, Freeman, et al., 1992).

Our work is related to two previous publications that learn image representations for use in compression. Gregor, Besse, et al. (2016) introduce an interesting hierarchical representation of images, in which degradations are more natural looking than those of linear representations. They derive discrete entropy estimates from the model by quantizing the learnt continuous representation, and obtain images at different entropy levels by eliminating parts of the representation. This is not likely to be optimal for the reasons outlined in section 2.1 (which the authors do acknowledge, stating that the discretization needs further "tuning"). Our end-to-end optimization methodology offers a more systematic way to handle the rate–distortion trade-off. Toderici et al. (2016) acknowledge the need to optimize for various operating points in the rate–distortion sense, and their formulation has the advantage over ours that a single representation is sought for all rate points (this is a topic we are currently exploring). However, it is not clear whether their formulation necessarily leads to rate–distortion optimality, and their empirical results seem to suggest that this is not the case.

We are currently testing systems that use simpler rectified-linear or sigmoidal nonlinearities, to determine how much of the performance and visual quality of our results is due to use of biologically-inspired joint nonlinearities. Preliminary results indicate that qualitatively similar results are achievable with other activation functions we tested, but that rectified linear units generally require a substantially larger number of model parameters to achieve the same rate–distortion performance as the GDN/IGDN nonlinearities, which might be an advantage for real-world implementation of our method (say, in embedded systems). The results may indicate that GDN/IGDN are more efficient for this particular task (producing better models with fewer stages of processing, as we found for density estimation; Ballé, Laparra, and Simoncelli, 2015). However, such conclusions are based on a limited set of experiments and should at this point be considered provisional. More generally, GDN/IGDN nonlinearities offer a multivariate generalization of a particular type of sigmoidal function. As such, we expect that some variant of a universal function approximation theorem should hold for them.

The rate–distortion objective may be seen as a particular instantiation of the general unsupervised learning or density estimation problems. Since the transformation to a discrete representation may be viewed as a form of classification, it is worth considering whether our framework offers any insights that might be transferred to more specific supervised learning problems, such as object recognition. For example, the additive noise used in the objective function as a relaxation of quantization might also serve the purpose of making supervised classification networks more robust to small perturbations, and thus allow them to avoid catastrophic failures that have been demonstrated in previous work (Szegedy et al., 2013). In any case, our results provide a strong example of the power of end-to-end optimization in achieving a new solution to a classical problem.

### Acknowledgments

We thank Olivier Hénaff and Matthias Bethge for fruitful discussions.

## References

Ballé, Johannes, Valero Laparra, and Eero P. Simoncelli (2015). "Density Modeling of Images Using a Generalized Normalization Transformation". In: *arXiv e-prints*. Presented at the 4th Int. Conf. for Learning Representations, 2016. arXiv:1511.06281.

— (2016). "End-to-end optimization of nonlinear transform codes for perceptual quality". In: *arXiv e-prints*. Presented at 2016 Picture Coding Symposium. arXiv:1607.05006.

Candès, Emmanuel J. and David L. Donoho (2002). "New Tight Frames of Curvelets and Optimal Representations of Objects with $C^2$ Singularities". In: *Comm. Pure Appl. Math.* 57, pp. 219–266.

Carandini, Matteo and David J. Heeger (2012). "Normalization as a canonical neural computation". In: *Nature Reviews Neuroscience* 13. DOI: 10.1038/nrn3136.

Deng, J. et al. (2009). "ImageNet: A Large-Scale Hierarchical Image Database". In: *IEEE Conf. on Computer Vision and Pattern Recognition*. DOI: 10.1109/CVPR.2009.5206848.

Gersho, Allen and Robert M. Gray (1992). *Vector Quantization and Signal Compression*. Kluwer. ISBN: 978-0-7923-9181-4.

Gray, Robert M. and David L. Neuhoff (1998). "Quantization". In: *IEEE Transactions on Information Theory* 44.6. DOI: 10.1109/18.720541.

Gregor, Karol, Frederic Besse, et al. (2016). "Towards Conceptual Compression". In: *arXiv e-prints*. arXiv:1604.08772.

Gregor, Karol and Yann LeCun (2010). "Learning Fast Approximations of Sparse Coding". In: *Proceedings of the 27th International Conference on Machine Learning*.

Heeger, David J. (1992). "Normalization of cell responses in cat striate cortex". In: *Visual Neuroscience* 9.2. DOI: 10.1017/S0952523800009640.

Jarrett, Kevin et al. (2009). “What is the Best Multi-Stage Architecture for Object Recognition?” In: *2009 IEEE 12th International Conference on Computer Vision*. DOI: 10.1109/ICCV.2009.5459469.

Kingma, Diederik P. and Jimmy Lei Ba (2014). “Adam: A Method for Stochastic Optimization”. In: *arXiv e-prints*. Presented at the 3rd Int. Conf. for Learning Representations, 2015. arXiv:1412.6980.

Kingma, Diederik P. and Max Welling (2014). “Auto-Encoding Variational Bayes”. In: *arXiv e-prints*. arXiv:1312.6114.

Laparra, Valero et al. (2016). “Perceptual image quality assessment using a normalized Laplacian pyramid”. In: *Proceedings of SPIE, Human Vision and Electronic Imaging XXI*.

Lewicki, Michael S. and Bruno A. Olshausen (1998). “Inferring sparse, overcomplete image codes using an efficient coding framework”. In: *Advances in Neural Information Processing Systems 10*, pp. 815–821.

Lyu, Siwei (2010). “Divisive Normalization: Justification and Effectiveness as Efficient Coding Transform”. In: *Advances in Neural Information Processing Systems 23*, pp. 1522–1530.

Marpe, Detlev, Heiko Schwarz, and Thomas Wiegand (2003). “Context-Based Adaptive Binary Arithmetic Coding in the H.264/AVC Video Compression Standard”. In: *IEEE Transactions on Circuits and Systems for Video Technology* 13.7. DOI: 10.1109/TCSVT.2003.815173.

Netravali, A. N. and J. O. Limb (1980). “Picture Coding: A Review”. In: *Proceedings of the IEEE* 68.3. DOI: 10.1109/PROC.1980.11647.

Oord, Aäron van den, Nal Kalchbrenner, and Koray Kavukcuoglu (2016). “Pixel Recurrent Neural Networks”. In: *arXiv e-prints*. arXiv:1601.06759.

Rezende, Danilo Jimenez, Shakir Mohamed, and Daan Wierstra (2014). “Stochastic Backpropagation and Approximate Inference in Deep Generative Models”. In: *arXiv e-prints*. arXiv:1401.4082.

Rippel, Oren, Jasper Snoek, and Ryan P. Adams (2015). “Spectral Representations for Convolutional Neural Networks”. In: *Advances in Neural Information Processing Systems 28*, pp. 2449–2457.

Rissanen, Jorma and Glen G. Langdon Jr. (1981). “Universal modeling and coding”. In: *IEEE Transactions on Information Theory* 27.1. DOI: 10.1109/TIT.1981.1056282.

Schwartz, Odelia and Eero P. Simoncelli (2001). “Natural signal statistics and sensory gain control”. In: *Nature Neuroscience* 4.8. DOI: 10.1038/90526.

Selesnick, Ivan W., Richard G. Baraniuk, and Nick C. Kingsbury (2005). “The Dual-Tree Complex Wavelet Transform”. In: *IEEE Signal Processing Magazine* 22.6. DOI: 10.1109/MSP.2005.1550194.

Shannon, Claude E. (1948). “A Mathematical Theory of Communication”. In: *The Bell System Technical Journal* 27.3. DOI: 10.1002/j.1538-7305.1948.tb01338.x.

Simoncelli, Eero P., William T. Freeman, et al. (1992). “Shiftable Multiscale Transforms”. In: *IEEE Transactions on Information Theory* 38.2. DOI: 10.1109/18.119725.

Simoncelli, Eero P. and Bruno Olshausen (2001). “Natural image statistics and neural representation”. In: *Annual Review of Neuroscience* 24. DOI: 10.1146/annurev.neuro.24.1.1193.

Sinz, Fabian and Matthias Bethge (2013). “What Is the Limit of Redundancy Reduction with Divisive Normalization?” In: *Neural Computation* 25.11. DOI: 10.1162/NECO_a_00505.

Szegedy, Christian et al. (2013). “Intriguing properties of neural networks”. In: *arXiv e-prints*. arXiv:1312.6199.

Theis, Lucas, Aäron van den Oord, and Matthias Bethge (2015). “A note on the evaluation of generative models”. In: *arXiv e-prints*. Presented at the 4th Int. Conf. for Learning Representations. arXiv:1511.01844.

Toderici, George et al. (2016). “Full Resolution Image Compression with Recurrent Neural Networks”. In: *arXiv e-prints*. arXiv:1608.05148.

Wang, Zhou, Eero P. Simoncelli, and Alan Conrad Bovik (2003). “Multi-Scale Structural Similarity for Image Quality Assessment”. In: *Conf. Rec. of the 37th Asilomar Conf. on Signals, Systems and Computers, 2004*. DOI: 10.1109/ACSSC.2003.1292216.

Wintz, Paul A. (1972). “Transform Picture Coding”. In: *Proceedings of the IEEE* 60.7. DOI: 10.1109/PROC.1972.8780.

## 6 Appendix

### 6.1 Network architecture and optimization

As described in the main text, our analysis transform consists of three stages of convolution, downsampling, and GDN – details of the architectural choices are provided in figure 8. These choices are somewhat ad-hoc, and a more careful exploration of alternative architectures could potentially lead to significant performance improvements.

We have previously shown that GDN is highly efficient in Gaussianizing the local joint statistics of natural images (Ballé, Laparra, and Simoncelli, 2015). Even though Gaussianization is a quite different optimization problem than the rate–distortion objective with the set of constraints defined above, it is similar in that we are assuming a marginally independent latent model in both cases. When optimizing for Gaussianization, the exponents in the parametric form of GDN control the tail behavior of the Gaussianized densities. Since tail behavior is less important here, we chose to simplify the functional form, fixing the exponents and forcing the weight matrix to be symmetric (i.e., $\gamma_{ij} = \gamma_{ji}$).

The synthesis transform is meant to function as an approximate inverse transformation, so we construct it by applying a principle known from the LISTA algorithm (Gregor and LeCun, 2010) to the fixed point iteration previously used to invert the GDN transform (Ballé, Laparra, and Simoncelli, 2015). We refer to this nonlinear transform as "inverse GDN" (IGDN). The full synthesis transform consists of three stages of IGDN, upsampling, and convolution, where the optimization of the synthesis parameters is untied from those used in the analysis stages.

The full model (analysis and synthesis filters, GDN and IGDN parameters) were optimized over a subset of the ImageNet database (Deng et al., 2009) consisting of 6507 images. We applied a number of preprocessing steps to the images from the database in order to reduce artifacts and other unwanted contaminations: first, we eliminated images with excessive saturation. We added a small amount of uniform noise, corresponding to the quantization of pixel values, to the remaining images. Finally, we downsampled and cropped the images to a size of $256 \times 256$ pixels each, where the amount of downsampling and cropping was randomized, but depended on the size of the original image. In order to reduce high-frequency noise and compression artifacts, the resampling factor was never permitted to be greater than 0.75; we discarded the images that were not large enough.

To ensure a fast and stable optimization, we used the following techniques:

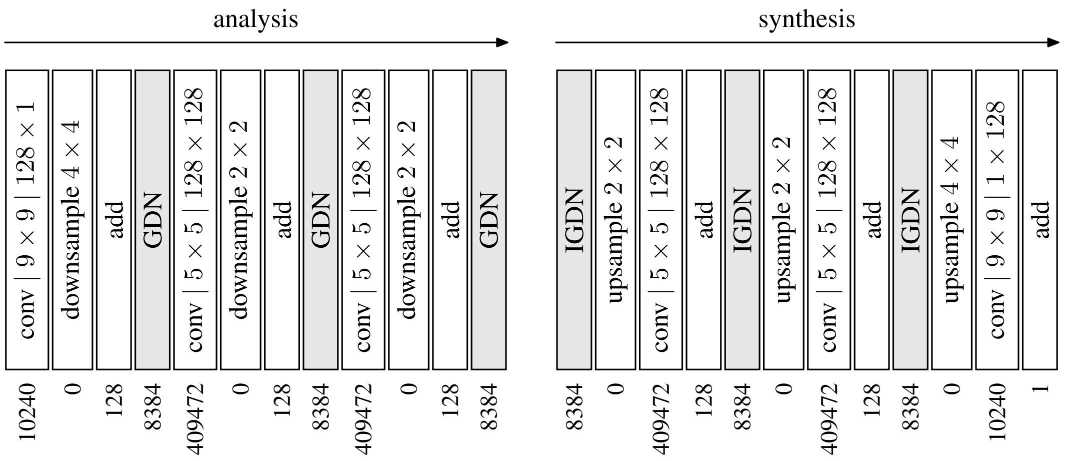

Figure 8: Architecture of synthesis ($g_s$) and analysis ($g_a$) transforms for grayscale images. *conv*: convolutional layer, with filter support (x×y) and number of feature maps (output×input). *down-/upsample*: regular down-/upsampling (by x×y factors, implemented jointly with the adjacent convolution). *add*: elementwise addition of a bias parameter per feature map. *GDN/IGDN*: generalized divisive normalization across feature maps (but not across space), and its approximate inverse; see text. Number of parameters for each layer given at the bottom.

- We used the Adam optimization algorithm (Kingma and Ba, 2014) to obtain values for the parameters $\boldsymbol{\phi}$ and $\boldsymbol{\theta}$, starting with $\alpha = 10^{-4}$, and subsequently lowering it by a factor of 10 whenever the improvement of both rate and distortion stagnated, until $\alpha = 10^{-7}$.
- We parameterized the linear filters using their discrete cosine transform (DCT) coefficients. We found this to be slightly more effective in speeding up the convergence than discrete Fourier transform (DFT) parameterization (Rippel, Snoek, and Adams, 2015).
- We parameterized the GDN/IGDN $\boldsymbol{\beta}$ parameters in terms of the elementwise relationship

  $$\beta_i = (\beta_i')^2 - 2^{-10}.$$

  This ensures that gradients are smaller around parameter values close to 0, a regime in which the optimization can otherwise become unstable. To ensure an unambiguous mapping, we projected each $\beta_i'$ onto the interval $[2^{-5}, \infty)$ after each gradient step. We applied the same treatment to the elements of $\boldsymbol{\gamma}$, and additionally averaged $\boldsymbol{\gamma}'$ with its transpose after each step in order to make it symmetric.
- To remove the scaling ambiguity between the each linear transform and its following nonlinearity (or preceding nonlinearity, in the case of the synthesis transform), we renormalized the linear filters after each gradient step, dividing each filter by the square root of the sum of its squared coefficients. For the analysis transform, the sum runs over space and all input feature maps, and for the synthesis transform, over space and all output feature maps.

We represented each of the marginals $p_{\tilde{y}_i}$ as a piecewise linear function (i.e., a linear spline), using 10 sampling points per unit interval. The parameter vector $\boldsymbol{\psi}^{(i)}$ thus simply consists of the value of $p_{\tilde{y}_i}$ at these sampling points. We did not use Adam to update $\boldsymbol{\psi}^{(i)}$; rather, we used ordinary stochastic gradient descent to minimize the negative expected likelihood:

$$L_\psi(\boldsymbol{\psi}^{(0)}, \boldsymbol{\psi}^{(1)}, \dots) = -\mathbb{E}_{\tilde{\boldsymbol{y}}} \sum_i p_{\tilde{y}_i}(\tilde{y}_i; \boldsymbol{\psi}^{(i)}). \tag{13}$$

and renormalized the marginal densities after each step. This yields unbiased running estimates of the marginal densities, unlike minimizing the loss function given in (5) over $\boldsymbol{\psi}^{(i)}$. After every $10^6$ gradient steps, we used a heuristic to adapt the range of the spline approximation to the values of $\tilde{y}_i$ that had been actually observed.

## 6.2 Entropy code

We implemented an entropy coder based on the context-adaptive binary arithmetic coding (CABAC) framework defined by Marpe, Schwarz, and Wiegand (2003). Arithmetic entropy codes are designed to compress discrete-valued data to bit rates closely approaching the entropy of the representation, assuming that the probability model used to design the code describes the data well. The following information was encoded into the bitstream:

- the size of the image (two 16-bit integers, bypassing arithmetic coding),
- whether the image is grayscale or RGB (one bit, bypassing arithmetic coding),
- the value of $\lambda$ (one 16-bit integer, bypassing arithmetic coding), which provides an index for the parameters of the analysis and synthesis transforms as well as the initial probability models for the discrete codes (these are learned during training, and assumed to be available to encoder and decoder).
- the value of each element of $\boldsymbol{q}$, iterating over feature maps, and over space in raster-scan order, using the arithmetic coding engine.

Since CABAC operates on binary values, the quantized values in $\boldsymbol{q}$ need to be converted to binary decisions. We follow a simple scheme inspired by the encoding of H.264/AVC transform coefficients as detailed by Marpe, Schwarz, and Wiegand (2003). For each $q_i$, we start by testing if the encoded value is equal to the mode of the distribution. If this is the case, the encoding of $q_i$ is completed. If not, another binary decision determines whether it is smaller or larger than the mode. Following that, each possible integer value is tested in turn, which yields a bifurcated chain of decisions as illustrated in figure 9. This process is carried out until either one of the binary decisions determines

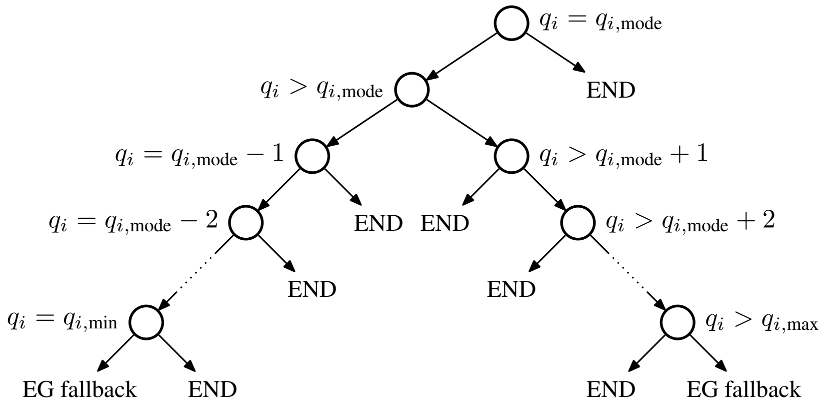

$q_i = q_{i,\text{mode}}$
END
$q_i > q_{i,\text{mode}}$
$q_i = q_{i,\text{mode}} - 1$
$q_i > q_{i,\text{mode}} + 1$
$q_i = q_{i,\text{mode}} - 2$
END
END
$q_i > q_{i,\text{mode}} + 2$
END
END
$q_i = q_{i,\text{min}}$
$q_i > q_{i,\text{max}}$
EG fallback
END
END
EG fallback

Figure 9: Binarization of a quantized value for binary arithmetic coding. Each circle represents a binary decision encoded with its own CABAC context. Arrows pointing left represent “false”, arrows pointing right “true”. On reaching END, the encoding of the quantized value is completed. On reaching EG fallback, the magnitude of $q_i$ which falls outside of the range $[q_{i,\text{min}}, q_{i,\text{max}}]$ is encoded using an exponential Golomb code, bypassing the arithmetic coding engine.

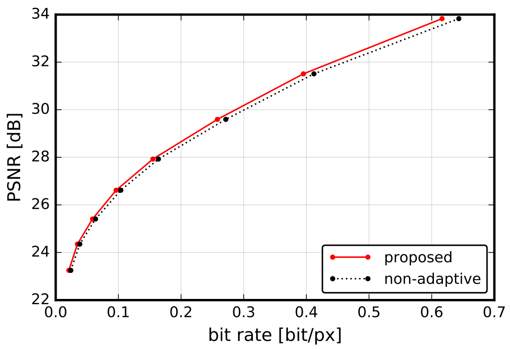

Figure 10: Rate–distortion comparison of adaptive vs. non-adaptive entropy coding, averaged (for each value of $\lambda$) over the 24 images in the Kodak test set. The non-adaptive entropy code is simulated by computing the entropy of $\boldsymbol{q}$ assuming the probability model learned during training (which is also used to initialize the adaptive code).

$q_i$, or some minimum ($q_{i,\text{min}}$) or maximum ($q_{i,\text{max}}$) value is reached. In case $q_i$ is outside of that range, the difference between it and the range bound is encoded using an exponential Golomb code, bypassing the arithmetic coding engine.

Adaptive codes, such as CABAC, can potentially further improve bit rates, and to some extent correct model error, by adapting the probability model on-line to the statistics of the data. In our code, this is achieved by sharing the marginal probability model $P_{q_i}$ of each element in $\boldsymbol{q}$ across space within each feature map. We derived the initial probability models by subsampling the continuous densities $p_{\tilde{y}_i}$ learned during training, as in (4). However, note that the coding scheme presented above only crudely exploits spatial adaptation of the probability model compared to existing coding methods such as JPEG 2000 and H.264/AVC. Thus, the performance gains compared to a well-designed non-adaptive entropy code are relatively small (figure 10), and likely smaller than those achieved by the JPEG 2000 coder to which we compare.

## 6.3 Evaluation details and additional example images

Although it is desirable to summarize and compare the rate–distortion behavior of JPEG, JPEG 2000 and our coder across an image set, it is difficult to do this in a way that is fair and interpretable. First, rate–distortion behavior varies substantially across bit rates for different images. For example, for the image in figure 12, our method achieves the same MSE with roughly 50% of the bits needed by JPEG 2000 for low rates, and about 30% for high rates. For the image in figure 17, the gains

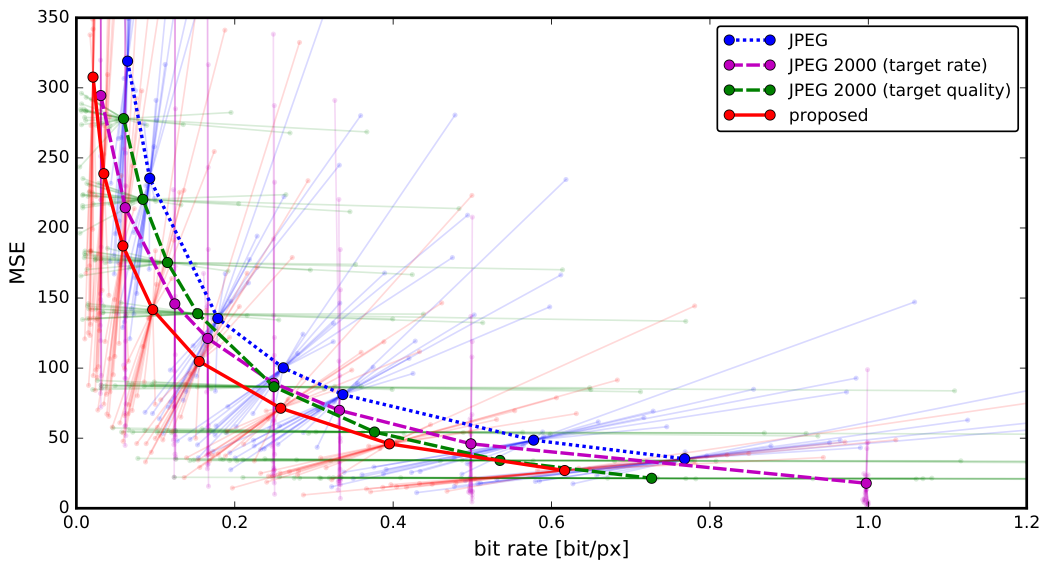

Figure 11: Summary rate–distortion curves, computed by averaging results over the 24 images in the Kodak test set. Each point is connected by translucent lines to the set of 24 points corresponding to the individual image R-D values from which it was derived. JPEG results are averaged over images compressed with identical quality settings. Results of the proposed method are averaged over images compressed with identical $\lambda$ values (and thus, computed with exactly the same forward and inverse transforms). The two JPEG 2000 curves are computed with the same coder, by averaging over images compressed with the same target rate or the same target quality. Note that these two methods of selecting points to be averaged lead to significantly different average results.

are more modest, although still significant through the range. But for the image in figure 15, our method only slightly outperforms JPEG 2000 at low rates, and under-performs it at high rates. These behaviors are different for MS-SSIM, which shows a significant improvement for all images and bitrates (consistent with their visual appearance).

Second, there is no obvious or agreed-upon method for combining rate–distortion curves across images. More specifically, one must decide which points in the curves to combine. For our coder, it is natural to average the MSE and entropy values across images compressed using the same choice of $\lambda$, since these are all coded and decoded using exactly the same representation and quantization scheme. For JPEG, it seems natural to average over images coded at the same "quality" setting, which appear to be coded using the same quantization choices. The OpenJPEG implementation of JPEG 2000 we use allows selection of points on the rate–distortion curve *either* through specification of a target bit rate, *or* a target quality. This choice has no effect on rate–distortion plots for a individual images (verified, but not shown), but has a substantial effect when averaging, since the two choices lead one to average over a different set of R-D points. This is illustrated in figure 11. Even if points were selected in exactly the same fashion for each of the methods (say, matched to a given set of target rates), summary plots can still over- or underemphasize high rate vs. low rate performance.

We conclude that summaries of rate–distortion are of limited use. Instead, we encourage the reader to browse our extensive collection of test images, with individual rate–distortion plots for each image, available at `http://www.cns.nyu.edu/~lcv/iclr2017` in both grayscale and RGB.

In the following pages, we show additional example images, compressed at relatively low bit rates, in order to visualize the qualitative nature of compression artifacts. On each page, the JPEG 2000 image is selected to have the lowest possible bit rate that is equal or greater than the bit rate of the proposed method. In all experiments, we compare to JPEG with 4:2:0 chroma subsampling, and the OpenJPEG implementation of JPEG 2000 with the default "multiple component transform". For evaluating PSNR, we use the JPEG-defined conversion matrix to convert between RGB and Y'CbCr. For evaluating MS-SSIM (Wang, Simoncelli, and Bovik, 2003), we used only the resulting luma component. Original images are not shown, but are available online, along with compressed images at a variety of other bit rates, at `http://www.cns.nyu.edu/~lcv/iclr2017`.

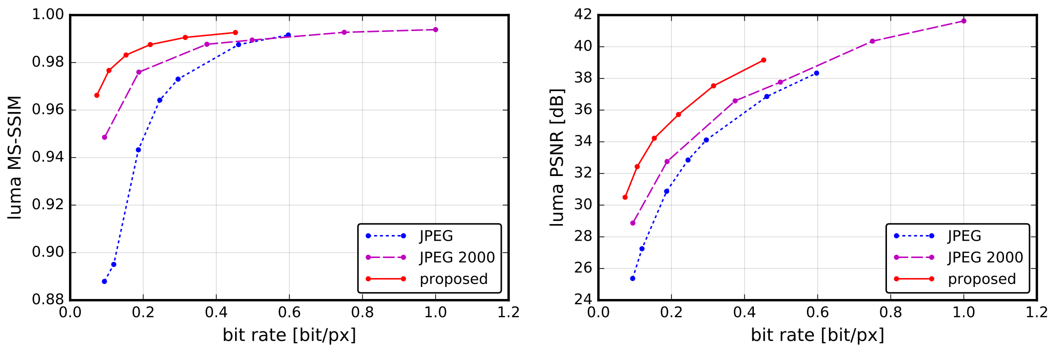

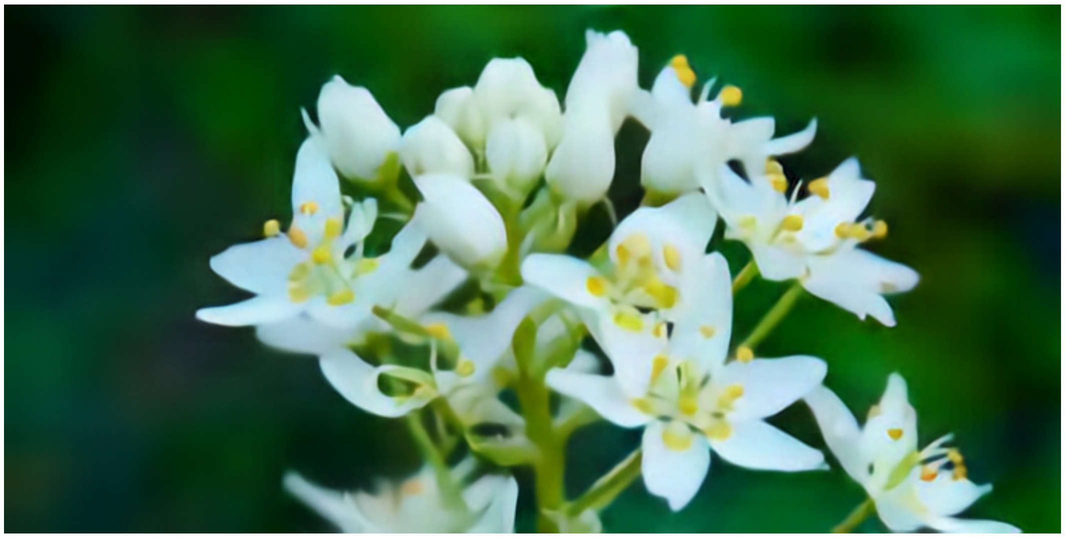
**Proposed method**, 3749 bytes (0.106 bit/px), PSNR: 32.43 dB/34.00 dB, MS-SSIM: 0.9767

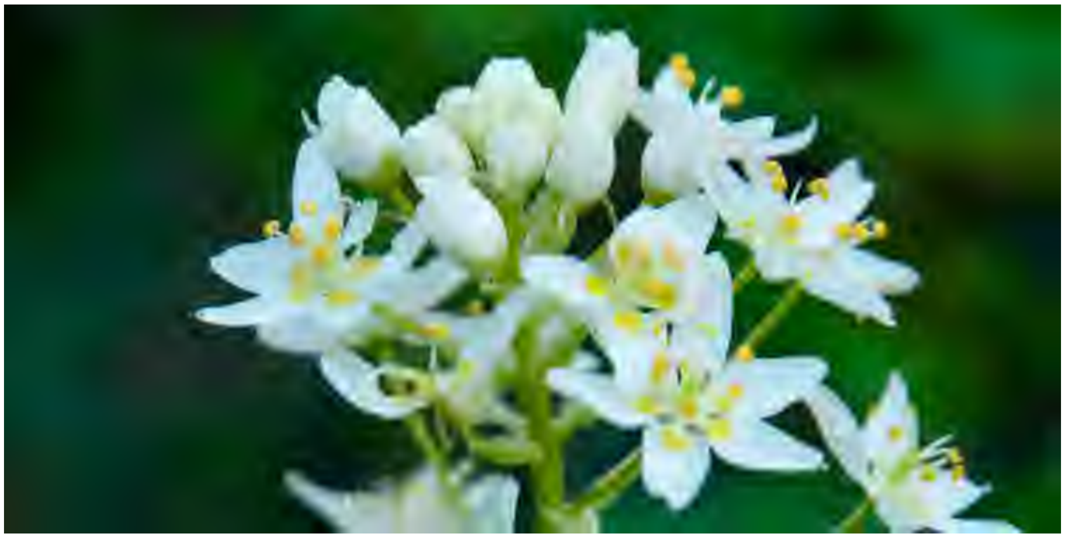
**JPEG 2000**, 3769 bytes (0.107 bit/px), PSNR: 29.49 dB/32.99 dB, MS-SSIM: 0.9520

Figure 12: RGB example, from our personal collection, downsampled and cropped to 752 × 376 pixels.

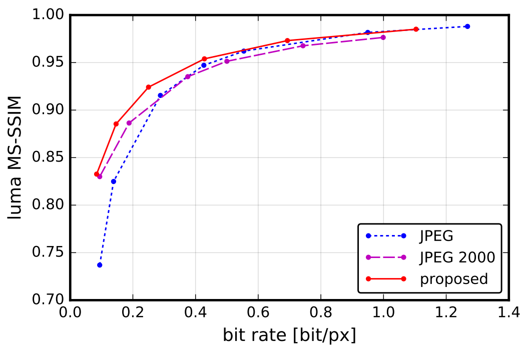

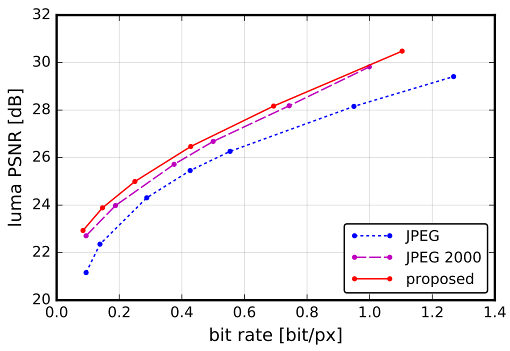

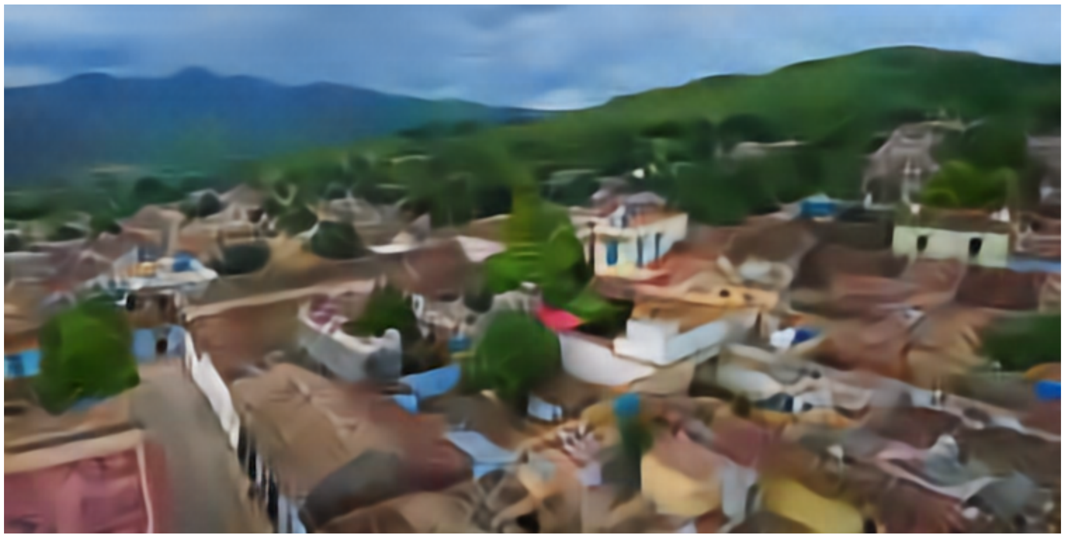

**Proposed method**, 2978 bytes (0.084 bit/px), PSNR: 22.93 dB/31.45 dB, MS-SSIM: 0.8326

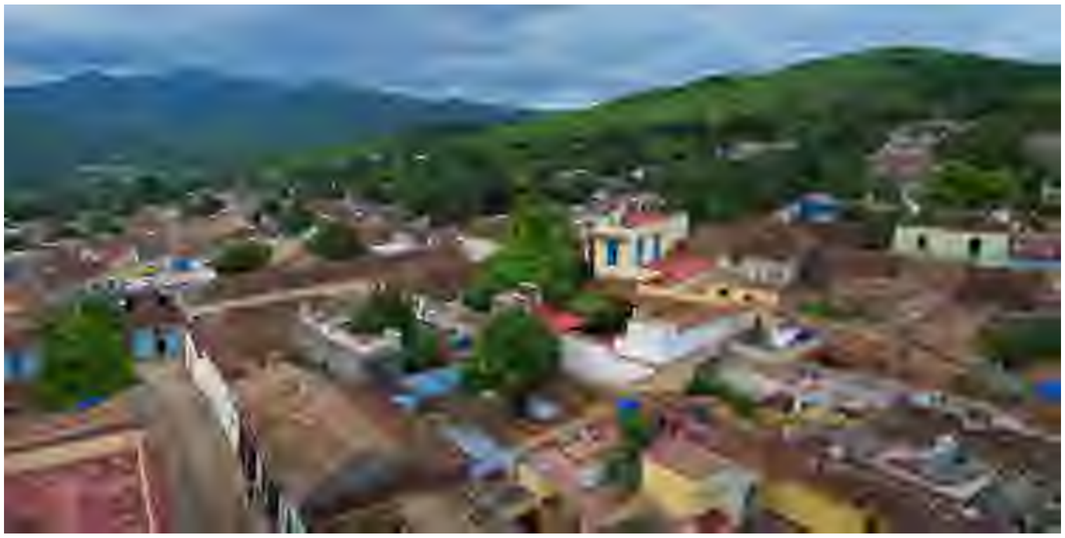

**JPEG 2000**, 2980 bytes (0.084 bit/px), PSNR: 22.53 dB/31.09 dB, MS-SSIM: 0.8225

Figure 13: RGB example, from our personal collection, downsampled and cropped to $752 \times 376$ pixels.

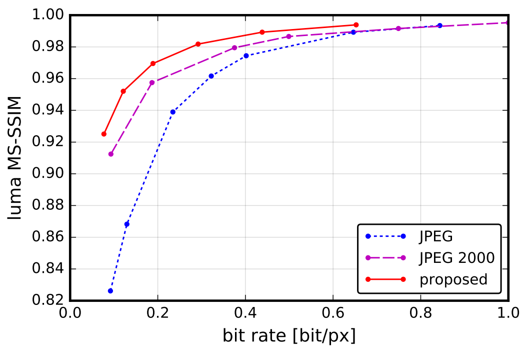

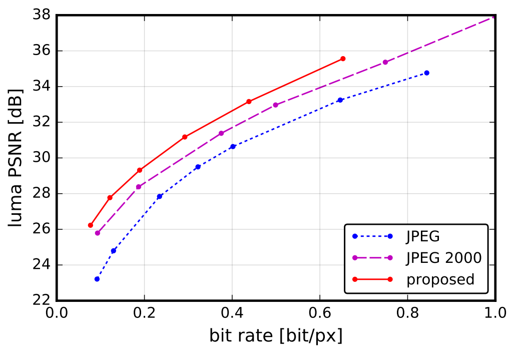

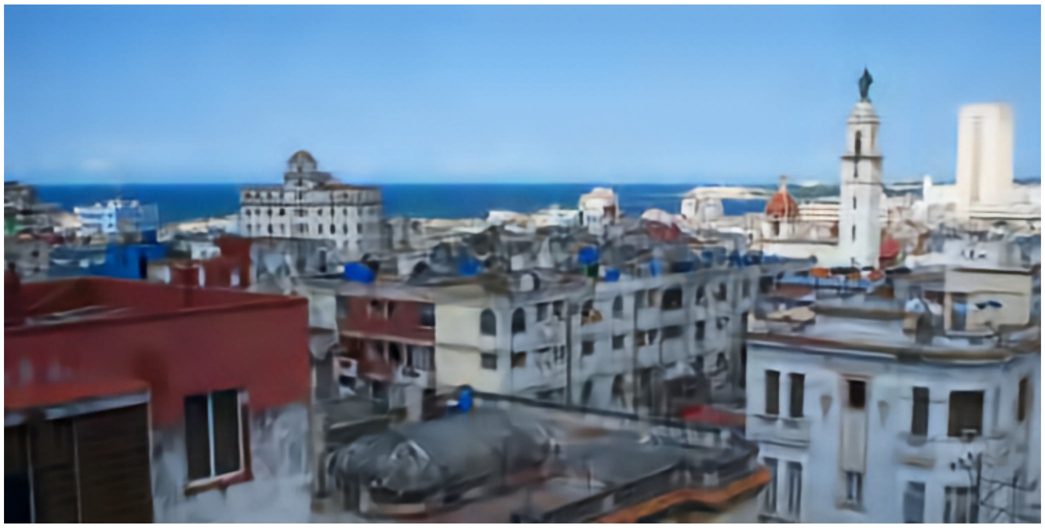
**Proposed method**, 6680 bytes (0.189 bit/px), PSNR: 29.31 dB/36.17 dB, MS-SSIM: 0.9695

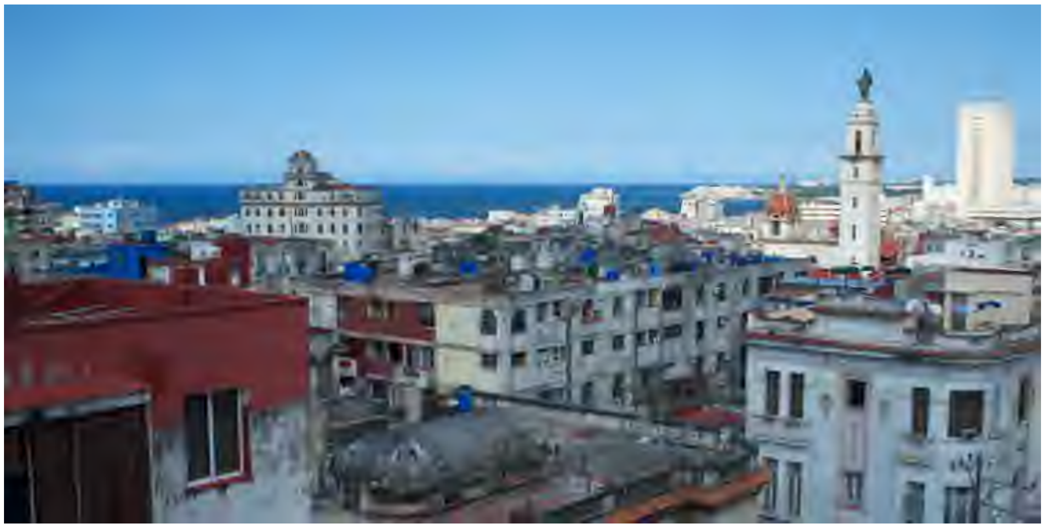
**JPEG 2000**, 6691 bytes (0.189 bit/px), PSNR: 28.45 dB/35.32 dB, MS-SSIM: 0.9586

Figure 14: RGB example, from our personal collection, downsampled and cropped to $752 \times 376$ pixels.

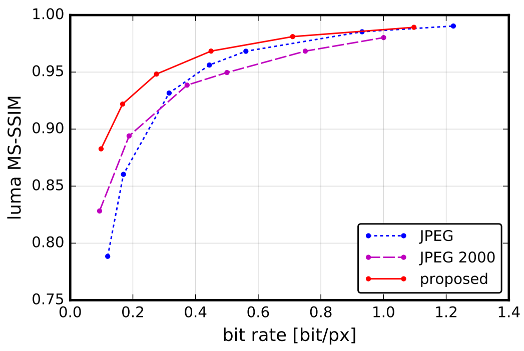

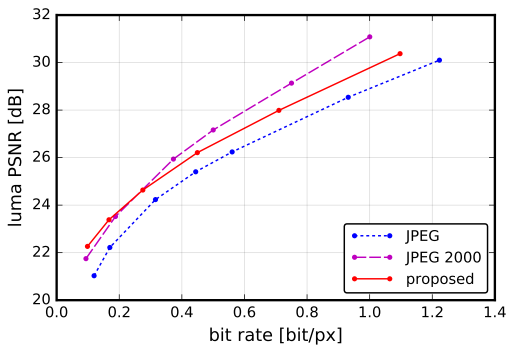

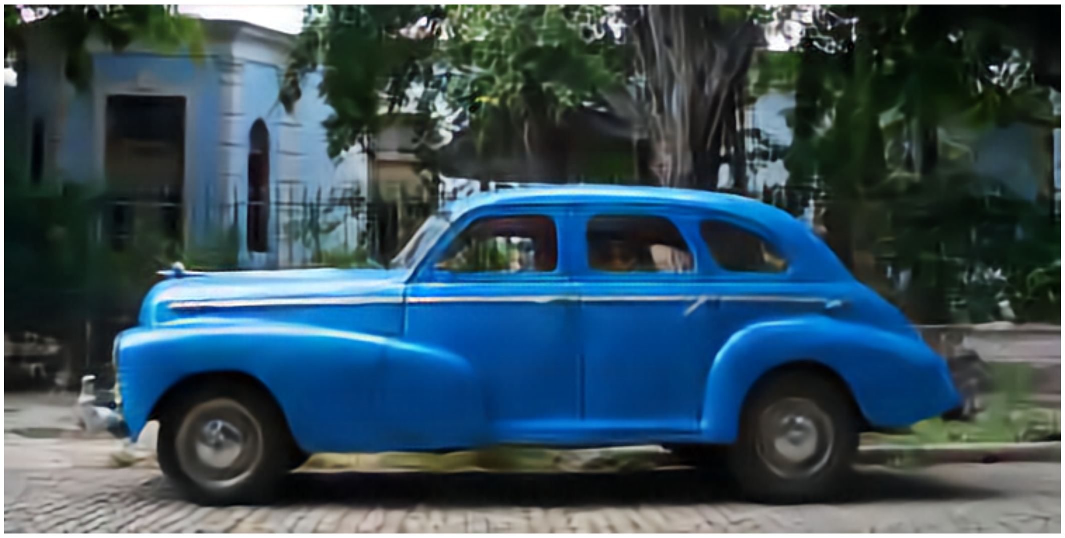

**Proposed method**, 5908 bytes (0.167 bit/px), PSNR: 23.38 dB/31.86 dB, MS-SSIM: 0.9219

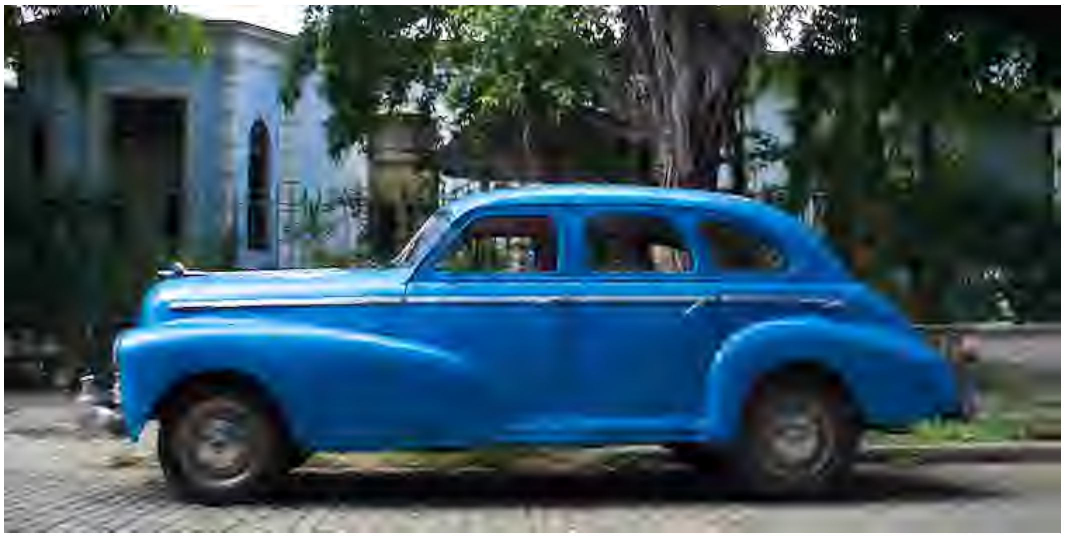

**JPEG 2000**, 5908 bytes (0.167 bit/px), PSNR: 23.24 dB/31.04 dB, MS-SSIM: 0.8803

Figure 15: RGB example, from our personal collection, downsampled and cropped to $752 \times 376$ pixels.

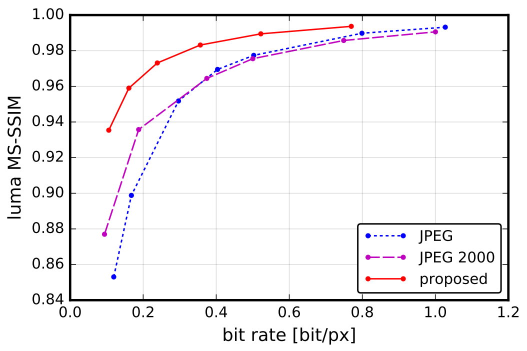

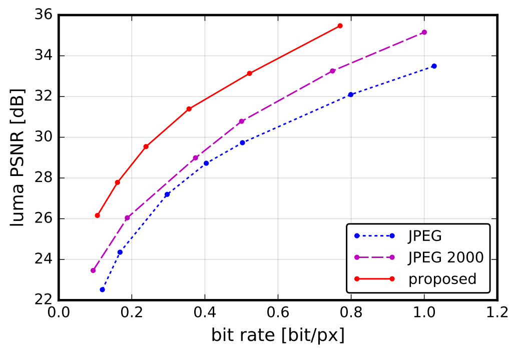

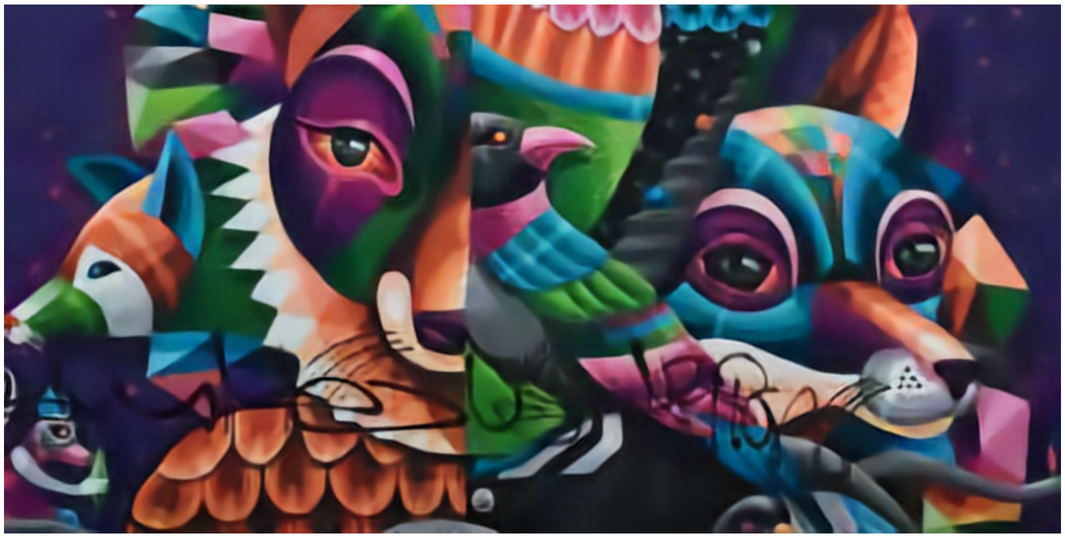
**Proposed method**, 5683 bytes (0.161 bit/px), PSNR: 27.78 dB/32.60 dB, MS-SSIM: 0.9590

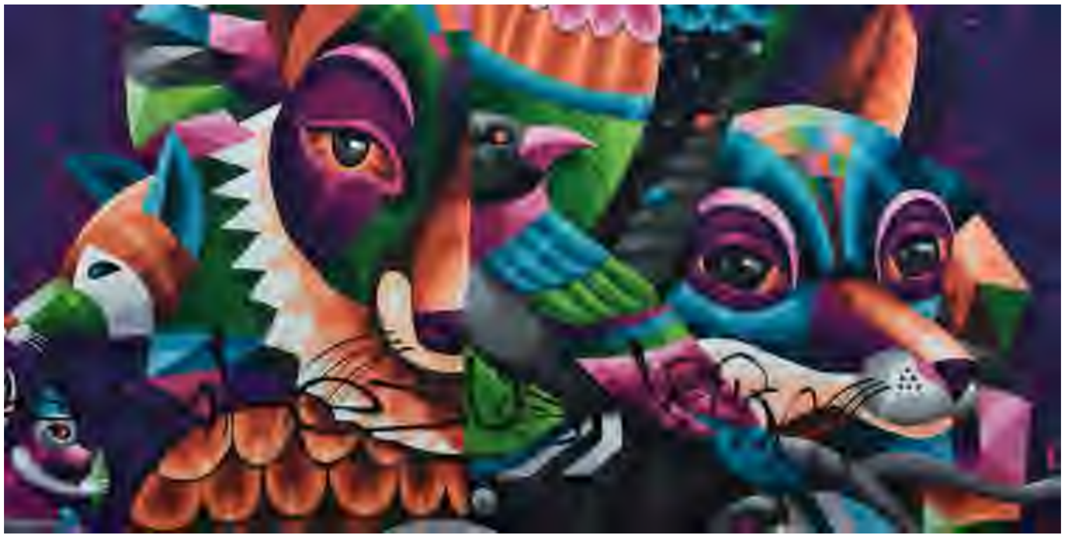
**JPEG 2000**, 5724 bytes (0.162 bit/px), PSNR: 25.36 dB/31.20 dB, MS-SSIM: 0.9202

Figure 16: RGB example, from our personal collection, downsampled and cropped to $752 \times 376$ pixels.

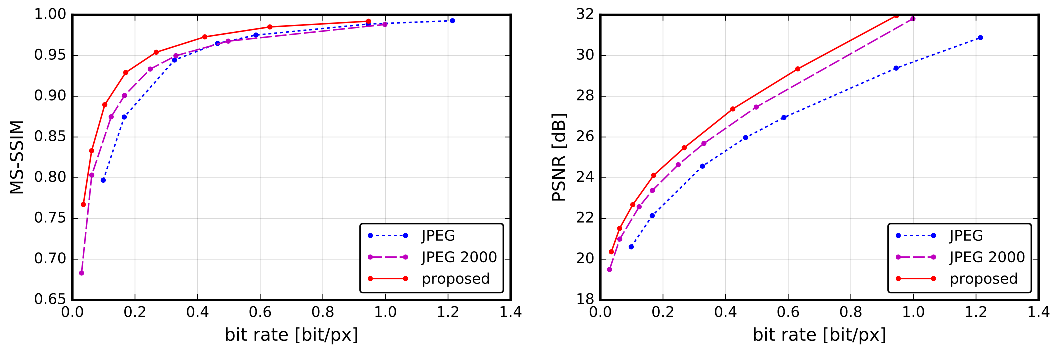

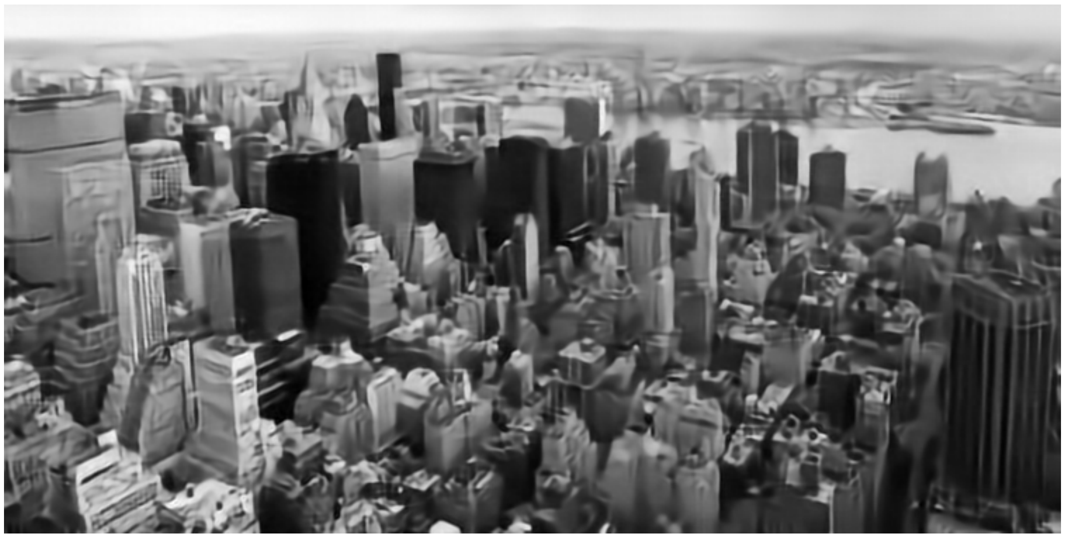

**Proposed method**, 6021 bytes (0.170 bit/px), PSNR: 24.12 dB, MS-SSIM: 0.9292

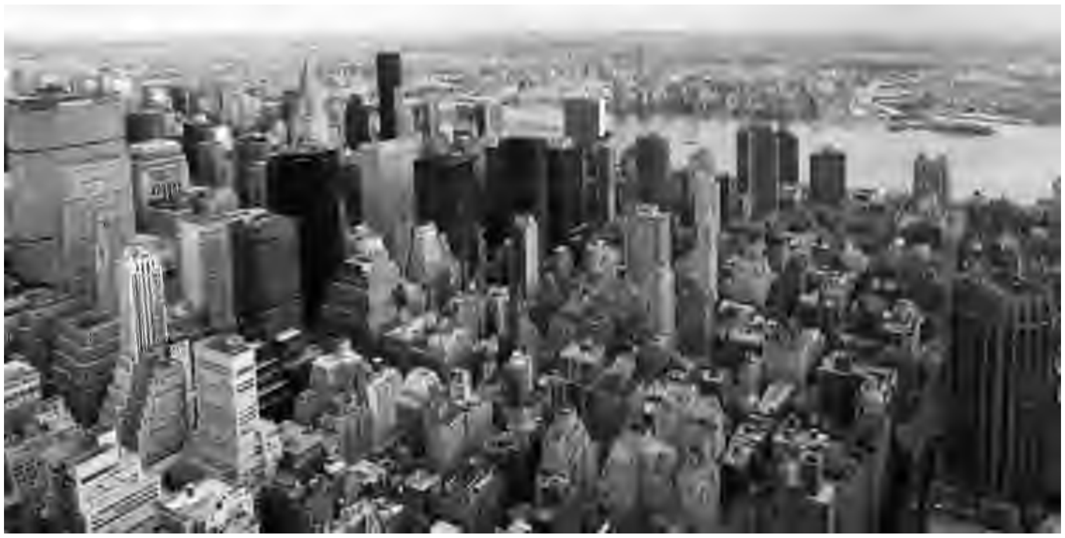

**JPEG 2000**, 6037 bytes (0.171 bit/px), PSNR: 23.47 dB, MS-SSIM: 0.9036

Figure 17: Grayscale example, from our personal collection, downsampled and cropped to 752×376 pixels.

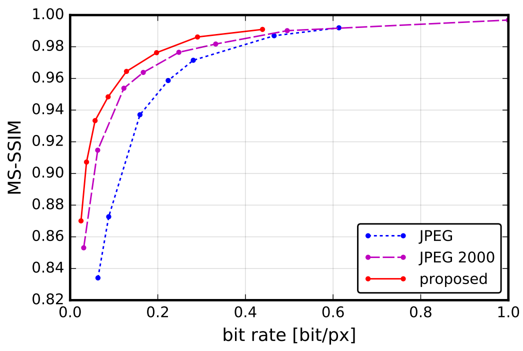

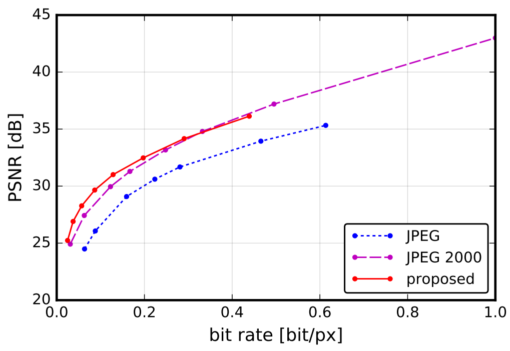

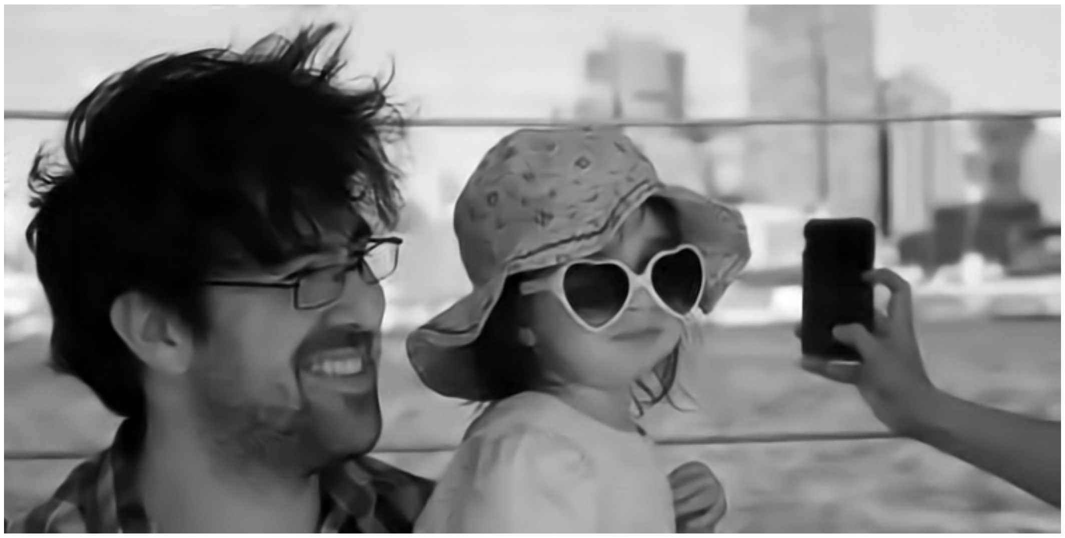

**Proposed method**, 4544 bytes (0.129 bit/px), PSNR: 31.01 dB, MS-SSIM: 0.9644

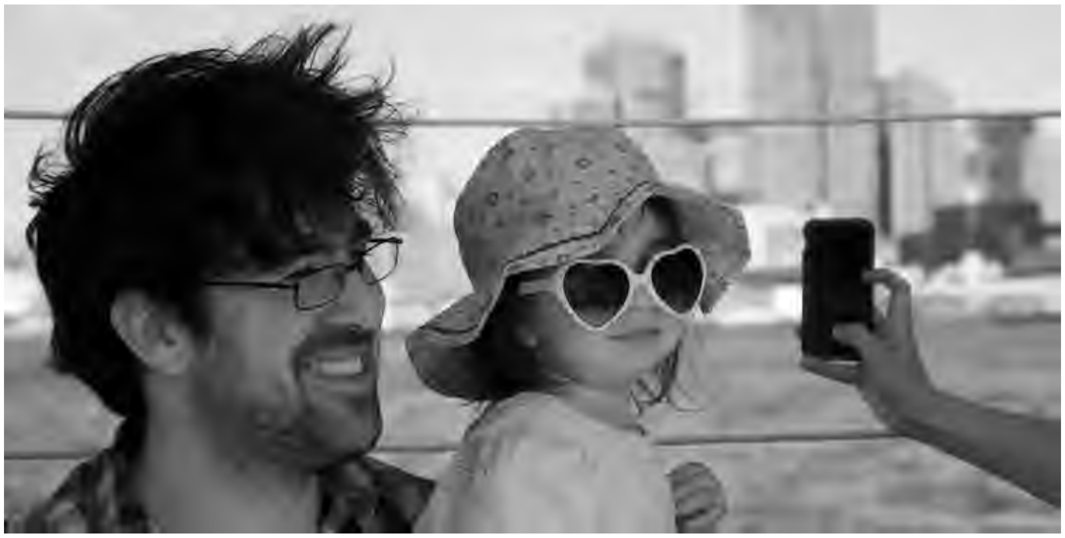

**JPEG 2000**, 4554 bytes (0.129 bit/px), PSNR: 30.17 dB, MS-SSIM: 0.9546

Figure 18: Grayscale example, from our personal collection, downsampled and cropped to 752 $\times$ 376 pixels.

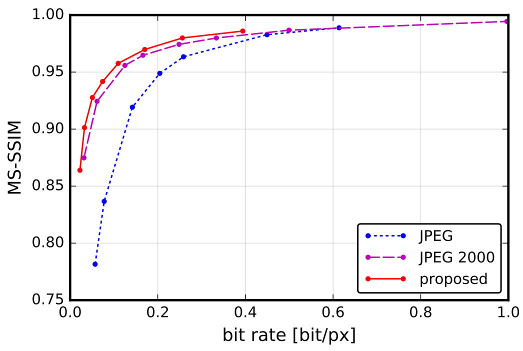

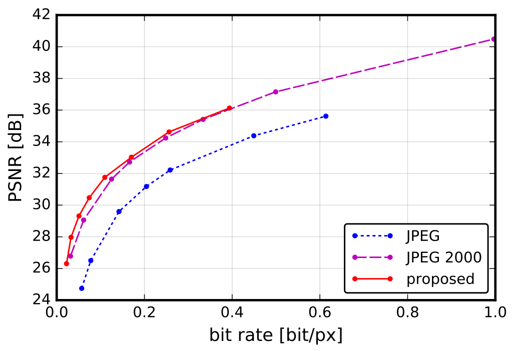

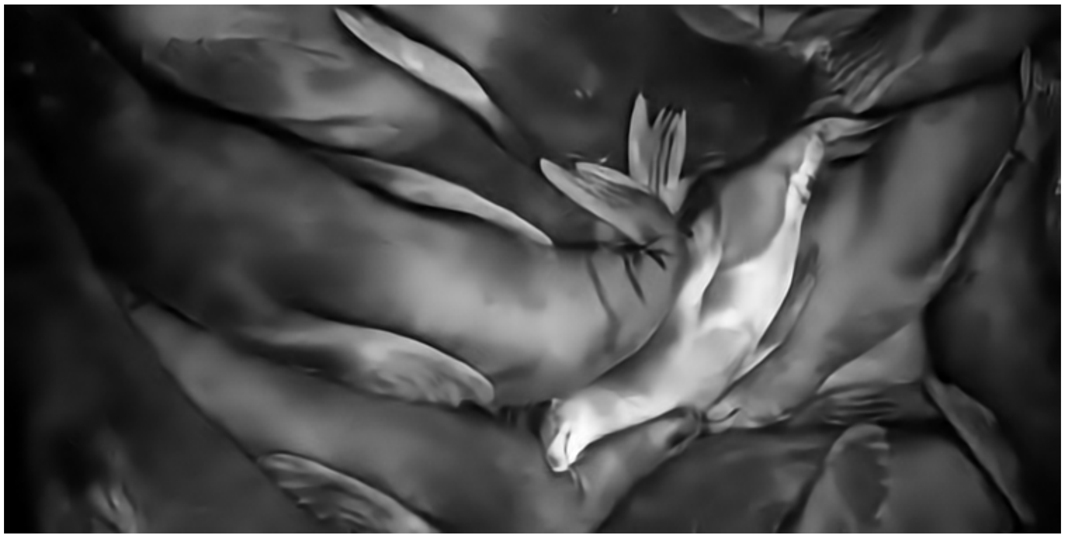

**Proposed method**, 3875 bytes (0.110 bit/px), PSNR: 31.75 dB, MS-SSIM: 0.9577

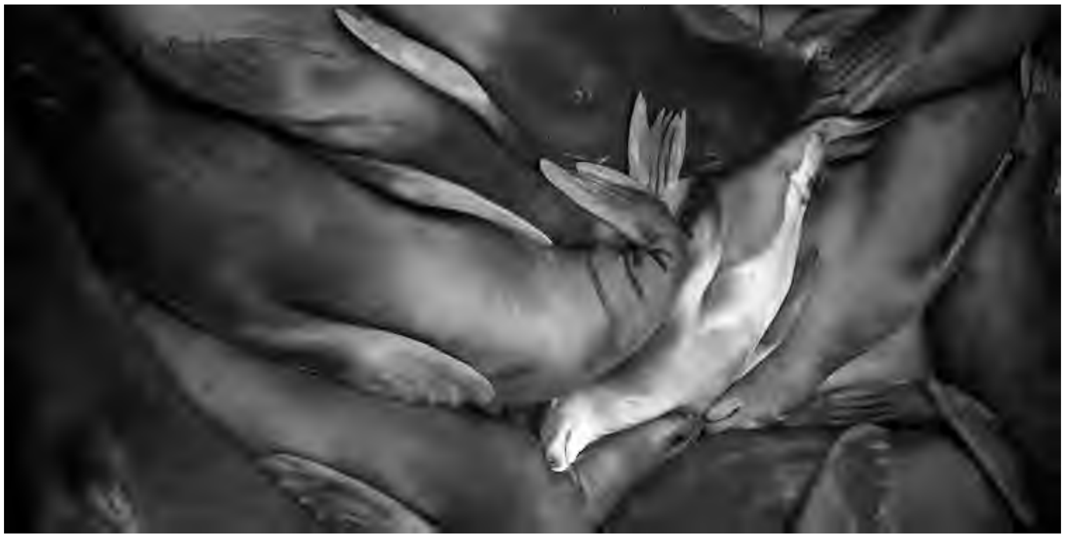

**JPEG 2000**, 3877 bytes (0.110 bit/px), PSNR: 31.24 dB, MS-SSIM: 0.9511

Figure 19: Grayscale example, from our personal collection, downsampled and cropped to $752\times376$ pixels.

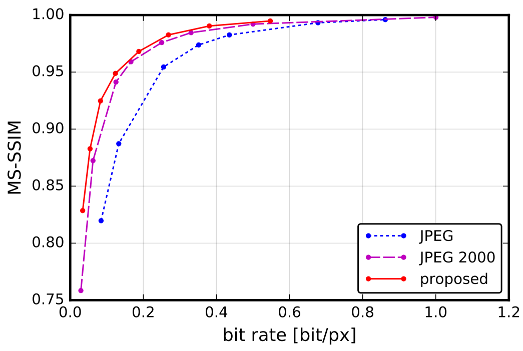

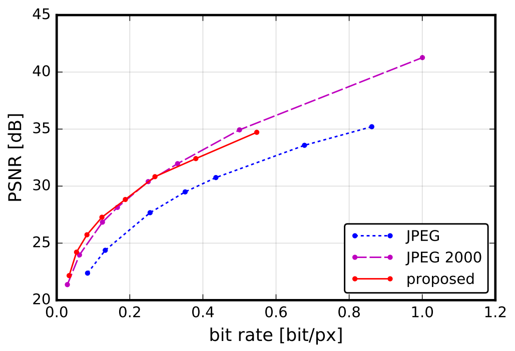

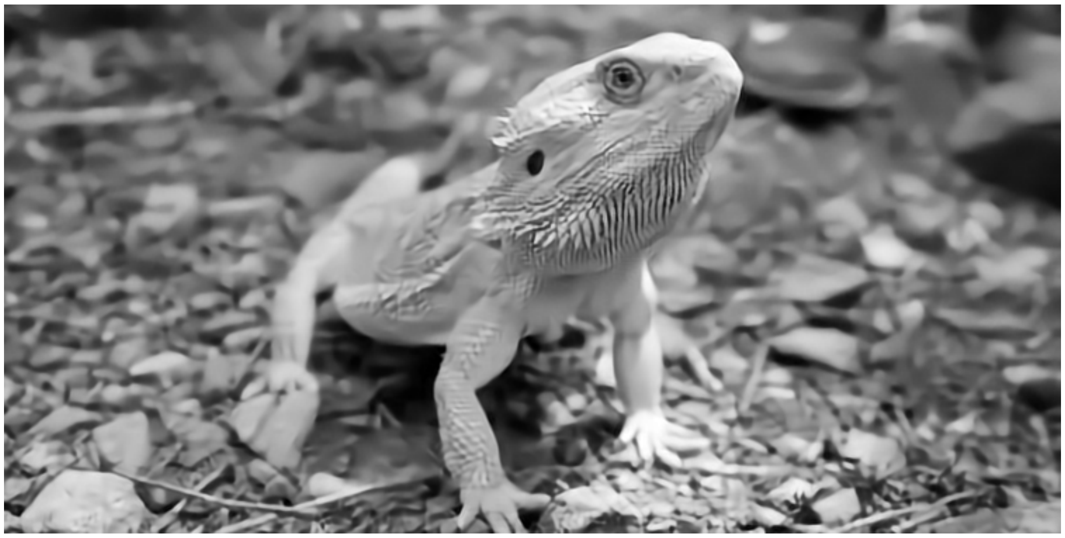
**Proposed method**, 6633 bytes (0.188 bit/px), PSNR: 28.83 dB, MS-SSIM: 0.9681

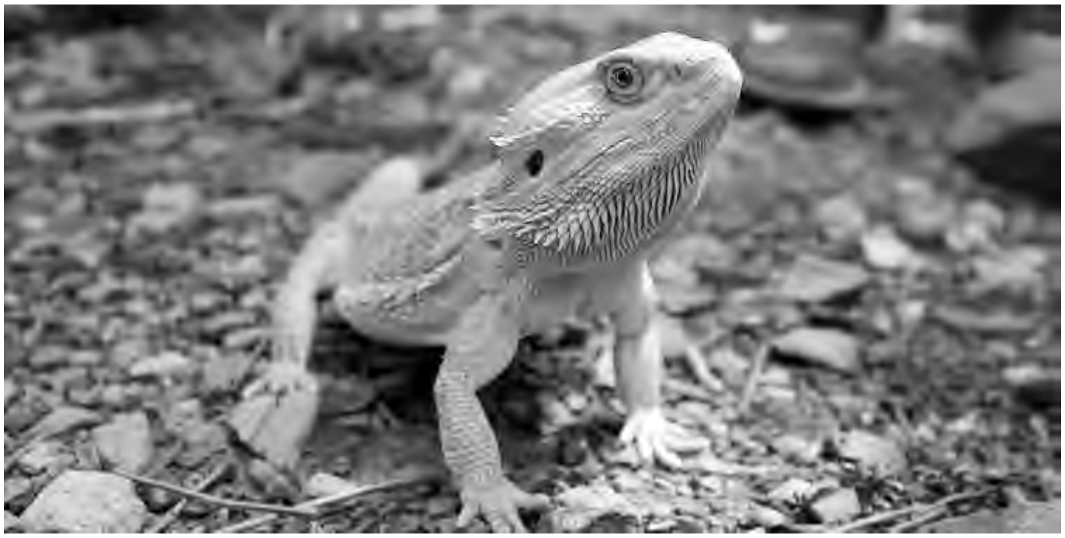
**JPEG 2000**, 6691 bytes (0.189 bit/px), PSNR: 28.83 dB, MS-SSIM: 0.9651

Figure 20: Grayscale example, from our personal collection, downsampled and cropped to $752 \times 376$ pixels.

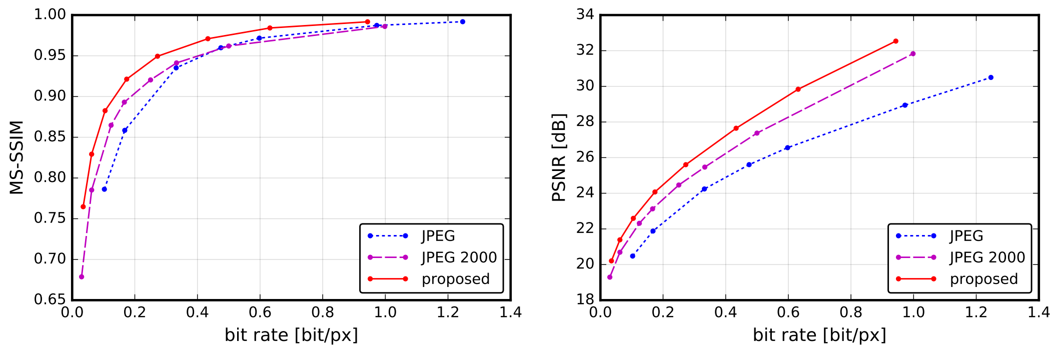

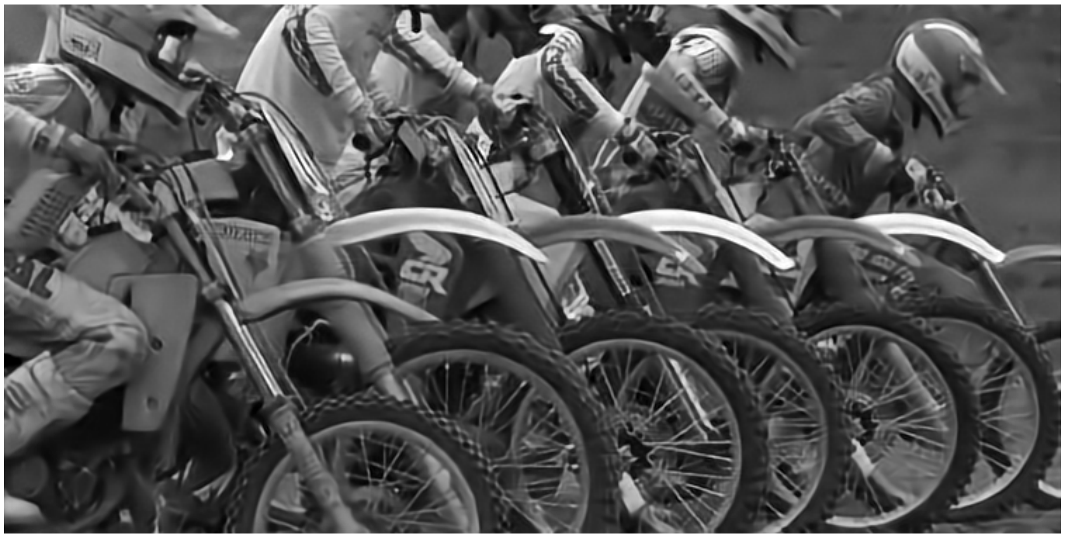
**Proposed method**, 10130 bytes (0.287 bit/px), PSNR: 25.27 dB, MS-SSIM: 0.9537

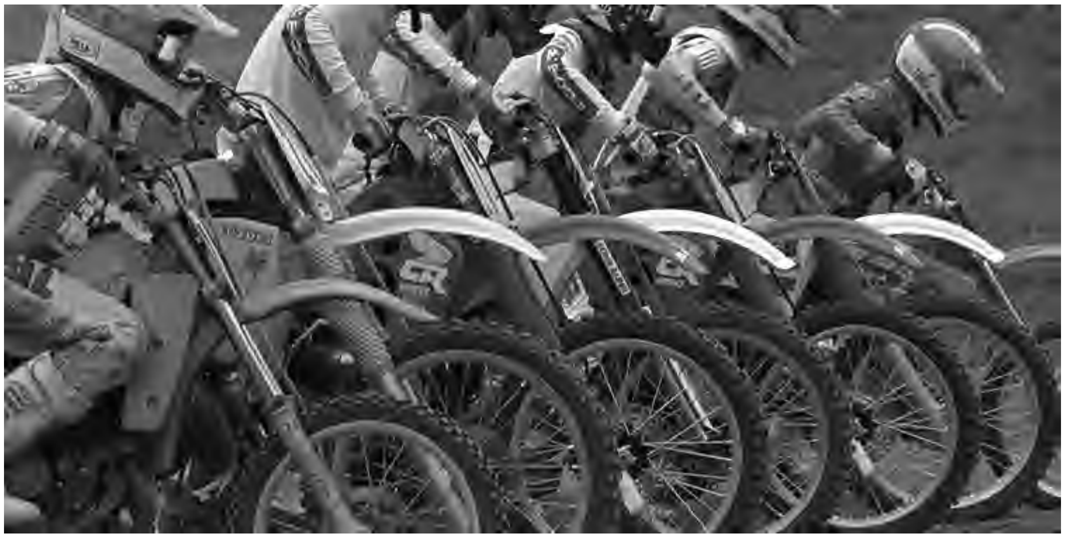
**JPEG 2000**, 10197 bytes (0.289 bit/px), PSNR: 24.41 dB, MS-SSIM: 0.9320

Figure 21: Grayscale example, from the Kodak test set, downsampled and cropped to 752 × 376 pixels.